Swansea University
Prifysgol Abertawe

The Effect of Copper and Tungsten Addition of the Passivity and Pitting Corrosion Resistance of Super Duplex Stainless Steels

Edward Purkhardt

Swansea University

Submitted to Swansea University in fulfilment of the requirements for the Degree of *Masters*

September 2023

Summary

The Critical Pitting Temperatures of Ferralium 255 (UNS S32550), Zeron 100 (UNS S32760), and SAF2507 (UNS S32750). were investigated to look at the effect of pH on the measured critical pitting temperature (CPT)and to understand the type of mechanism driving the formation and growth of the pits. Due to the elevated copper concentration in Ferralium alloy compared to the other alloys and, the elevated tungsten concentration in the SAF2507 (SAF) alloy compared to the alloys. The effect of copper and tungsten addition on the measured CPT could also be investigated.

An investigation into the effect of the pH of the test solution on the three alloys was conducted. All three alloys underwent a CPT test sweep at 4pH, 7pH and 10pH.

A clear difference was measured in the CPT of the individual alloys, they all had a measurable and notable difference in measured breakdown temperature. This consisted of the copper rich alloy (Ferralium) having an average CPT of 76^{o}C across the three tested pH solutions. The low copper alloy (Zeron) having the next highest measured CPT of 85^{o}C. With the tungsten rich alloy (SAF) having the highest measured CPT of 89^{o}C.

SEM imaging of the pits that formed found that the pits that had formed in all of the CPT sweeps for all of the alloys had formed a pit structure known as lacy capped pits. This cap on the pit is likely to enable concentrations of the solution on the internal of the pit to be high enough to encourage corrosion of the highly corrosion resistance super duplex stainless steels. There is no visible difference in the structure of the lacy capped pit formed in the individual alloys.

Time-lapse imagery (TLI) of the samples undergoing CPT sweeps was conducted to confirm that the pits were forming after the alloy transitioned through its critical temperature. The measured CPT of the individual alloys were consistent with those measured in the previous 3 investigations. The TLI was

able to capture the formations of the pits as the material transitioned through its critical temperature. It is possible that re-passivation of the pits were captured in the TLI. The re-passivation is likely to be caused by the lacy caps of the pits being removed or degrading. The loss of the cap results in the internal environment of the pit to no-longer be conducive to continuation of the corrosion reaction.

Declarations

This work has not previously been accepted in substance for any degree and is not being concurrently submitted in candidature for any degree.

Signed. [redacted] .....

Date 23/09/2023 .....

This thesis is the result of my own investigations, except where otherwise stated. Other sources are acknowledged by footnotes giving explicit references. A bibliography is appended.

Signed. [redacted] .....

Date 23/09/2023 .....

I hereby give consent for my thesis, if accepted, to be available for electronic sharing.

Signed [redacted] .....

Date 23/09/2023 .....

The University's ethical procedures have been followed and, where appropriate, that ethical approval has been granted.

Signed. [redacted] .....

Date 23/09/2023 .....

Contents

Acknowledgements

I would like to thank my academic supervisor Dr Natalie Wint for her support and guidance during my research. I would also like to thank my industrial supervisor Mr Rodney Rice for his recommendations, support, and interest in the project. I am very thankful for the help and support provided by Professor James Sullivan and Professor Geraint Williams during the progress of the research.

Definitions and Abbreviations

Super duplex stainless steel……. SDSS

Duplex stainless steel……... DSS

Stainless steel…….. SS

Open circuit potential……... OCP

Pitting potential…… Ep

Critical pitting temperature…….. CPT

Time Lapse Imaging ……..……..…….. TLI

Scanning Electron Microscopy…… SEM

Saturated calomel electrode…….. SCE

Gibbs free energy…….. ΔG

Gibbs free energy of activation……. ΔG*

Standard hydrogen electrode…….……...…..SHE

1.0 Literature Review

1.1 Corrosion Theory

Corrosion is a pervasive and costly process that affects many different metals and their alloys. It is an electrochemical reaction that causes the gradual deterioration and degradation of materials. The study of corrosion and its underlying mechanisms is important in industry to extend the life of products and components and to improve safety and reliability.

Corrosion poses significant economic, safety, and environmental challenges. It can compromise the integrity and reliability of critical structures and components. Understanding the fundamental principles and mechanisms of corrosion is essential to prevent and control the process of corrosion.

In this literature review the factors influencing corrosion, the different forms of corrosion and the electrochemical reactions that drive the process will be explored. The concept of the electrochemical cell involving anodic and cathodic reactions plays a central role in corrosion.

1.1.1 Basic Electrochemical Cell

The electrochemical cell is based on the redox (reduction-oxidation) reactions, with electrons transferring between electrodes immersed in an electrolyte solution. Each of the two half-cells contain an electrode and an electrolyte, connected by an external circuit. An electrode is an electrically conductive material that interacts with the electrolyte solution and the electrolyte is a conducting solution that contains ions. (1)

The basic electrochemical cell is the mechanism that enables various electrochemical devices including batteries, fuel cells and electrolysis cells. These devices use the redox reactions to convert chemical energy into electrical energy or use electrical energy to drive a chemical process. (2)

The difference in the electrode potentials between the anode and the cathode is known as the cell potential. It is a measure of electricity generated by the electrochemical cell. The cell potential is governed by the nature of the redox reaction and the concentrations of the species involved.

One half-cell contains the anode, and the other half-cell contains the cathode. The anode is the electrode where oxidation occurs, it releases electrons into the external circuit and generates positively charged metal ions in the electrolyte solution. The cathode is the electrode where reduction takes place. It receives electrons from the external circuit and causes metal ions from the electrolyte solution to gain electrons and deposit as metal atoms or compounds. (1) (2)

The anode and cathode are connected through the metal and the electrolyte creating a closed circuit that allows the flow of electrons from the anode to the cathode. As the electrons move through the circuit, an electrical current is generated, this is because electrical current is defined as the flow of electrons.

1.1.2 Electrochemistry of Corrosion

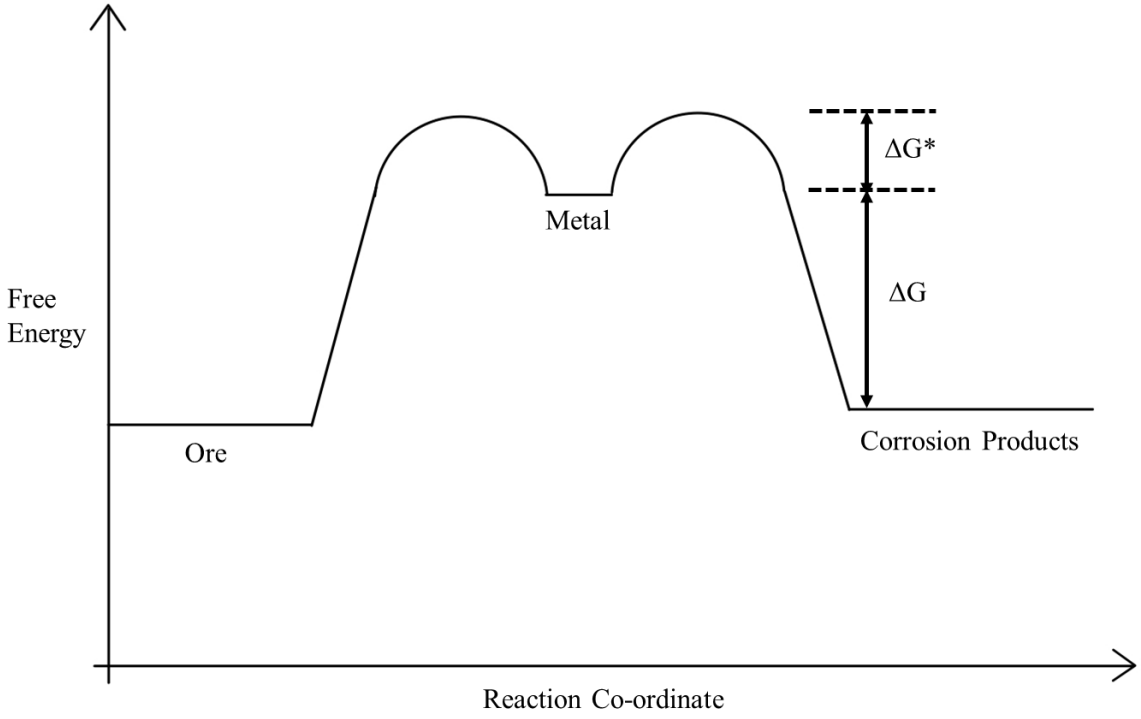

Figure 1.1: Gibbs free energy diagram of a metal, where ΔG is the free energy of activation.*

Gibbs free energy can be used as a measure of a material in different states. For example, in **Figure 1.1** a metal in its original 'Ore' state has a low free energy and is very stable. By increase the free energy of the material and going over the 'hump' or activation energy we are able to promote the material to a new form, in this case a 'metal'. The material is now in what is referred to as a meta stable position, as the material will not spontaneously change state due to activation energy requirement. If we put more energy into the metal system we are able to overcome the free energy of activation allowing the material to return to a stable position of 'corrosion products'.

Gibbs free energy depends only on the initial and final states of a system and is independent of the path taken to reach those states. For a closed system at constant temperature and pressure, the change in Gibbs free energy (ΔG) during

a chemical reaction is related to the work done by the system and the heat exchange with the surroundings. (3)

For a process to be spontaneous, the Gibbs free energy change (ΔG) must be negative ($\Delta G < 0$). This indicates that the process can occur without external intervention and releases energy to the surroundings. Conversely, if $\Delta G > 0$, the process is non-spontaneous and requires an input of energy to proceed.

At equilibrium, the Gibbs free energy change is zero ($\Delta G = 0$). This means the system has reached a stable state, and no net change occurs in the system.

Gibbs free energy also helps determine the maximum amount of work that can be extracted from a system. In chemical reactions, it provides information about whether a reaction will initiate under certain conditions. (3) (4)

Figure 1.1 shows an example of the Gibbs free energy diagram of a metal as it is refined into a metal, by increase its Gibbs free energy. The metal settles into a state of equilibrium, and as shown by the hump before dropping to the corrosion products there is a ΔG^* (free energy of activation) function. This energy of activation is required to transform the metal from its metallic state into its corrosion products. When the metal is in a state of ‘ore’ or ‘corrosion product’ is has the lowest available free energy, these states are therefore referred to as being stable. As the metal state is in an elevated level of free energy however is in equilibrium, requiring ΔG^* input for it to change state, it is referred to as being metastable. (4)

1.1.3 Electrochemical Series

The electrochemical series is a list of elements and their respective electrode potentials (E°). It is a fundamental concept in electrochemistry that ranks elements based on their tendency to undergo oxidation or reduction reactions in an electrochemical cell. A table showing an example of such a series is shown in Table 1.1. The series provides valuable information about the relative

strength of reducing or oxidizing agents and helps predict the feasibility of redox reactions. (5)

In the electrochemical series, elements are arranged in order of decreasing electrode potential shown in **Table 1.1**. The Standard Hydrogen Electrode (SHE) is typically used as the reference electrode and its potential is defined as 0 volts in the electrochemical series, **Table 1.1**. Elements with more positive electrode potentials are more likely to undergo reduction (gain electrons), while those with more negative electrode potentials are more likely to undergo oxidation (lose electrons).

The most active elements are located at the bottom of the series have the most negative electrode potentials and are highly reactive. They tend to lose electrons easily and are strong reducing agents. (6) (5)

The least active elements near the top of the series have the most positive electrode potentials and are least reactive. They are stable in their elemental

Table 1.1: The Electrochemical Series

Electrode Reaction	**E^0/V**
$Au^+ + e = Au$	+ 1.68
$Pt^{2+} + 2e = Pt$	+ 1.20
$Cu^{2+} + 2e = Cu$	+ 0.34
$2H^+ + 2e = H_2$	0.00
$Sn^{2+} + 2e = Sn$	- 0.14
$Ni^{2+} + 2e = Ni$	- 0.25
$Fe^{2+} + 2e = Fe$	- 0.44
$Cr^{3+} + 3e = Cu$	- 0.71
$Zn^{2+} + 2e = Zn$	- 0.76
$Al^{3+} + 3e = Al$	- 1.67
$Mg^{2+} + 2e = Mg$	- 2.34
$Na^+ + e = Na$	- 2.71
$Ca^{2+} + 2e = Ca$	- 2.87

form and have a higher affinity for gaining electrons. Noble metals like gold (Au), platinum (Pt), and silver (Ag) are good examples.

1.1.4 Passive Layers in Stainless Steels

Passive layers are present in stainless steels as a thin protective film of chromium oxide. The layer forms on the surface of a metal when it is exposed to oxygen in the atmosphere. This passive layer is what gives stainless steels their name and provides it with its corrosion resistance properties. (7) (8)

The passive layer is normally composed of chromium oxide (Cr_2O_3) and is typically a few nanometres thick. It forms when the chromium in stainless steel reacts with oxygen to create a stable, tightly adhered chromium oxide film on the surface. Amongst other factors, the concentration of chromium in the stainless steel alloy determines the quality and effectiveness of the passive layer. Higher chromium content leads to a more robust and corrosion-resistant passive layer. Stainless steel is classified into different grades based on its chemical composition. (7) (9)

The passive layer in stainless steel can be affected by certain environmental conditions or chemical exposures. For example, chlorides (from seawater or certain cleaning agents) can break down the passive layer and lead to corrosion of the stainless steel. If the passive layer is damaged or disrupted due to abrasion or corrosive chemical attack, the chromium present in the stainless steel will react with any available oxygen to reform the protective oxide film. The passive layer is highly stable and resistant to corrosion from a wide range of chemicals and environmental conditions. It acts as a barrier, preventing corrosive agents from coming into direct contact with the underlying metal. (9) (8)

1.1.5 Crevice Corrosion

Crevice corrosion is a localised form of corrosion that occurs in narrow gaps, or crevices, between two surfaces in contact with each other. A crevice can be formed when a gap is formed between two metal surfaces, such as two metal plates. This gap can be the result of imperfect fits, rough surfaces, gasket materials, or any other situation that creates a confined space where fluid (usually an electrolyte, like salt water) can become stagnant or trapped. (10)

The confined nature of the crevice restricts the flow of oxygen into the gap. As a result, the oxygen concentration within the crevice is reduced compared to the surrounding area. Due to variations in oxygen availability different regions within the crevice can have varying electrochemical potentials. This sets up a situation where the metal behaves as both anodes and cathodes, leading to the formation of an electrochemical corrosion cell. Anodes form where the local concentration of oxygen is reduced such as within the geometry of a crevice and hence this leads to localised anodic attack in these regions. The stagnant solution within the crevice can accumulate corrosive agents like chloride ions, which can accelerate the corrosion process. (10) (11)

The crevice corrosion process can lead to the breakdown of the passive film within the crevice area. The corrosion reaction can create pits or grooves, leading to significant material loss and structural damage over time.

Crevice corrosion is particularly problematic because it can occur in hidden or hard-to-reach areas, making detection and prevention challenging. It is commonly found in industrial equipment such as; heat exchangers, piping systems, and marine structures. (11) (12)

1.1.6 Pitting Corrosion Mechanism

Pitting corrosion is another localised and highly destructive form of corrosion that occurs on the surface of metals. It is characterised by the formation of small, deep pits or cavities that penetrate the metal. (13)

The mechanism of pitting corrosion involves several stages:

Initiation - Pitting corrosion typically starts with the breakdown or weakening of the passive film on the metal surface. Certain environmental conditions, such as the presence of aggressive ions like chloride ions or exposure to acidic solutions, can lead to breakdown of this protective film in specific areas on the metal surface. (13)

Anodic Reaction - Once the passive film is compromised, specific areas on the metal surface become anodic sites. These sites have a higher electrochemical potential than the surrounding metal, which means they tend to lose electrons more easily. As a result, they become more susceptible to corrosion.

Formation of Anodic Pits - At the anodic sites, metal atoms dissolve into metal ions (e.g., Fe^{2+} for iron) and release electrons into the metal. The metal ions then migrate into the surrounding electrolyte (usually water with dissolved ions). As the metal ions leave the metal surface, small pits start to form. These pits act as the anodic sites for further corrosion, leading to a self-sustaining corrosion process. (13) The anodic attack is further exacerbated by the differential aeration, reduction in oxygen concentration, caused by the geometry of the pit.

Concentration Effect - The presence of the pit concentrates aggressive ions (e.g., chloride ions) and other corrosive agents within the confined space. The high concentration of these agents further accelerates the corrosion process within the pit.

Cathodic Reaction - Simultaneously, on the metal surface outside the pits, a cathodic reaction occurs. Oxygen reduction or the reduction of hydroxide ions (from water) take place, consuming the electrons released by the anodic pits.

Enhanced Corrosion - The combination of anodic and cathodic reactions creates a galvanic cell within and around the pit. This results in accelerated metal dissolution within the pit, causing it to grow deeper and wider over time. (13) (14)

The process of pitting corrosion continues, leading to the formation of numerous pits on the metal surface. The pits can grow rapidly, and if not detected and controlled, they can cause severe damage to the metal structure, leading to leaks, fractures, or failure. A diagram depicting the mechanism can be seen in **Figure 1.2**.

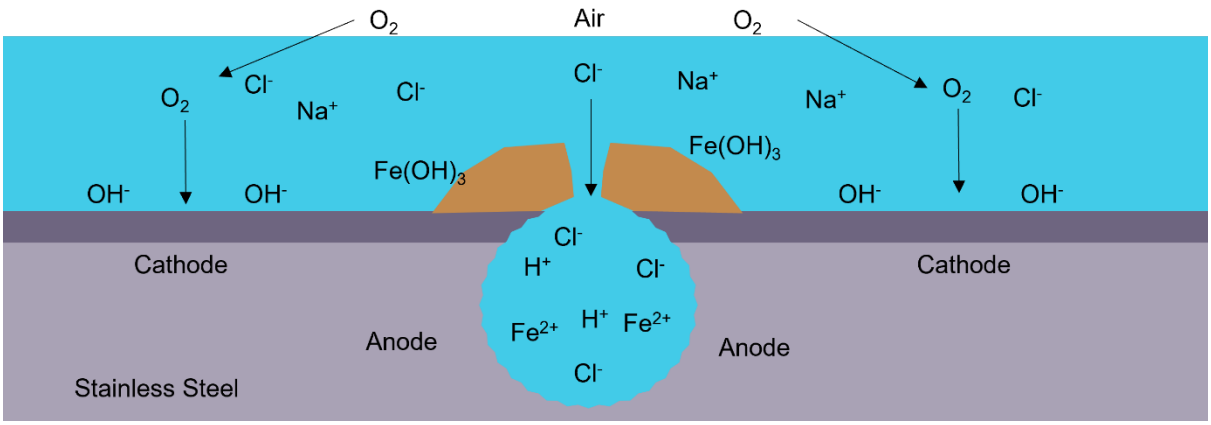

Figure 1.2: Diagram an example of the mechanisms present during pitting corrosion of a stainless steel. (Dark grey layer representing the passive layer)

1.1.7 Pourbaix Diagram

A Pourbaix diagram is a graphical representation of the thermodynamic stability of a chemical species, in a solution as a function of its voltage potential (E) and pH. It is used to predict the stability of different materials and can provide information on their behaviour under different environmental conditions. (15)

The diagram is a plot with the x-axis representing the pH of the solution and the y-axis representing the electrode potential (Eh) of the system. The potential is measured relative to a reference electrode, commonly the Standard Hydrogen Electrode (SHE). (16) (17)

Each point on the Pourbaix diagram corresponds to a specific combination of pH and potential, and it is associated with different chemical species of the element or metal in the solution. These chemical species can be in various oxidation states and forms.

Different regions in the Pourbaix diagram correspond to the stability of different phases of the element or metal under certain conditions. The diagram helps determine whether the metal is in a stable or metastable state, or whether it is prone to corrosion or is passivated (protected by a surface layer in the given pH and potential range).

The Pourbaix diagram is a powerful tool for understanding the behaviour of metals and elements in electrochemical systems, especially in corrosion studies and the design of protective coatings. A Pourbaix diagram can be used help to predict the behaviour of metals in different environments and to select suitable materials for specific applications (15). An example Pourbaix diagram is shown below showing Iron in a water system in **Figure 1.3**.

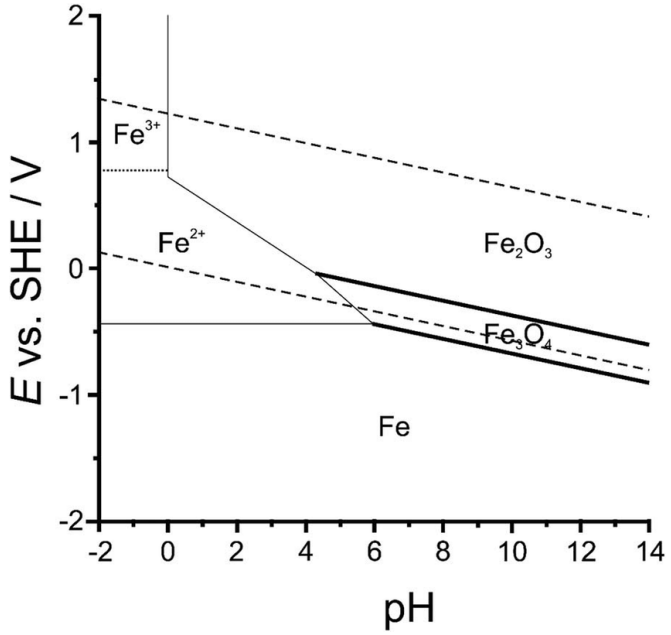

Figure 1.3: Example Pourbaix diagram depicting Iron in water. (21)

1.1.8 Reference Electrodes

A standard reference electrode (SRE) is a type of electrode used in corrosion assessments to provide a stable and reproducible reference potential, for comparison with other electrodes. SREs are often used in conjunction with other types of electrodes namely, working electrodes (often the sample under test)

and counter electrodes (often an inert material like platinum). The use of these electrodes enable measurement of corrosion rates and assess the effectiveness of corrosion mitigation strategies. Using an SRE, a working electrode and a counter electrode together is known as a three electrode setup. (18)

The most used SRE in corrosion assessments is the saturated calomel electrode (SCE), which consists of a silver/silver chloride electrode immersed in a solution of saturated potassium chloride and a small amount of mercurous chloride. The SCE has a well-defined potential of +0.241 V versus the standard hydrogen electrode (SHE) at 25°C and is stable over a wide range of temperatures and pH values. (18)

The SCE is typically used as a reference electrode in a three-electrode configuration, where it is connected to the working electrode and counter electrode in a cell containing the test solution. The potential difference between the SCE and the working electrode is measured using a potentiostat or other electrochemical instrumentation. The difference in potential can provide insights into the corrosion behaviour of the materials under test. (18)

The use of a standard reference electrode in corrosion assessments is essential for ensuring the accuracy and reproducibility of corrosion measurements. By providing a stable reference potential, SREs enable researchers to compare the corrosion behaviour of different materials under standardized conditions, helping to guide the selection of materials and the design of corrosion-resistant structures. (18)

1.1.9 Critical Pitting Temperature

The Critical Pitting Temperature (CPT) of stainless steels is a parameter that characterises the resistance of alloys to pitting corrosion. The Critical Pitting Temperature is the lowest temperature at which a stainless steel alloy becomes susceptible to pitting corrosion in specific corrosive environments, typically in chloride-containing solutions. Below the CPT, the passive film that forms on

the stainless steel surface remains stable, protecting it from pitting. However, above the CPT, the passive film may break down or become less effective, leading to the initiation and propagation of pits. (19) (20)

Several factors influence the Critical Pitting Temperature of stainless steels. The alloy's chemical composition, microstructure, and the concentration of aggressive ions (such as chloride ions) in the surrounding environment can have a large effect on the CPT behaviour of the material.

Stainless steels with higher CPTs are preferred for applications where they will be exposed to chloride-containing environments, such as marine environments and chemical processing facilities. These steels provide a higher level of corrosion resistance, preventing the initiation and progression of pitting corrosion at elevated temperatures or in aggressive conditions. (20)

1.1.10 Open Circuit Potential

Open-circuit potential (OCP) is used to characterise the corrosion behaviour of metals. It refers to the electrical potential difference that exists between a metal and a reference electrode when no external current is flowing. (6) (1)

Open-circuit potential plays a significant role in understanding the corrosion behaviour of metals, it provides insights into the thermodynamic driving force for electrochemical reactions at the metal surface. The open-circuit potential is a result of the balance between the anodic and cathodic reactions occurring on the metal surface. (1)

When certain metals or alloys have a protective layer, protecting the metal from corrosion, the open-circuit potential is relatively low and stable an which shows a high resistance to corrosion. (21)

If the metal surface is not covered by a protective passive film, the open-circuit potential will be in the active region. In this region, the metal is actively

corroding, and the open-circuit potential may fluctuate as the anodic and cathodic reactions occur.

In some environments, when the potential reaches a critical value, the passive film may break down, and the open-circuit potential enters the transpassive region. In this region, the metal may undergo a form of corrosion or pitting corrosion. (21)

Measurement of the open-circuit potential is a common technique in electrochemical studies, especially in corrosion experiments and corrosion monitoring. By monitoring the open-circuit potential over time, it is possible to determine the corrosion behaviour of metals and evaluate the effectiveness of corrosion protection strategies or the stability of passive films in specific environments. (21)

1.1.11 Time-lapse Imaging of Critical Pitting Temperature

Critical pitting temperature (CPT) experiments are typically conducted to evaluate the resistance of metallic materials to pitting corrosion. Timelapse imaging is a technique that can provide real-time insights into the onset and progression of pitting corrosion during CPT experiments. (22) (23) (24)

Recent studies have used timelapse imaging to investigate the effect of temperature and solution concentration on the pitting behaviour of steels of varying compositions. Timelapse imaging can provide insights into the mechanisms that govern pitting corrosion and improve the design of corrosion-resistant materials. (22) (25) (26)

1.1.12 Lacy Capped pits

Lacy cap pit formation is a type of localized corrosion that can occur on the surface of metals in the presence of chloride ions. It is characterised by the formation of pits that have a lace-like or spider web-like appearance. The formation of lacy cap pits is initiated by the adsorption of chloride ions on the

metal surface, which creates a localised area of increased acidity. This localised acidification can then lead to the dissolution of the metal and the formation of pits. The formation of the pits is believed to be due to a combination of factors, including the accumulation of corrosion products changes in the pH of the surrounding solution, and the presence of surface-active species. (27)

Literature has proposed a mechanism for the formation of lacy cap pits which suggests first a pit must initiate. Then, due to a change in concentration of ions vs the bulk solution, re-passivation of the edges of the pit occurs. The corrosion continues to occur in the centre of the pit which in turn undercuts the passivated area. Then the corrosion eats through the cap of the pit which then allows the release of ions from inside the pit back into the bulk electrolyte. Thus, the cycle repeats. A schematic on the mechanism is shown in **Figure 1.4**. (28)

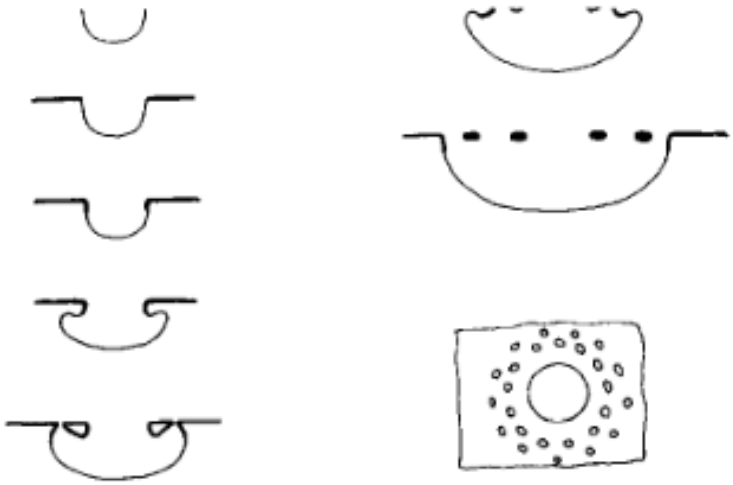

Figure 1.4: Proposed mechanism for lacy cap formation. (Passive surfaces are indicated by thick lines)

1.1.13 Scanning Electron Microscopy

Scanning Electron Microscopy is a characterisation technique that uses focused electrons to image small length scale features on samples, micron to nano metre. The imaged material is required to conduct electrons in order to be imaged. Secondary electron detection (SE) involves collecting emitted electrons from the surface of the sample which result from the primary, focused electron beam,

interacting with the material. SE imaging provides topographical information of the sample revealing surface morphology and texture. The technique is widely used in materials development and investigation to look at surface defects such as pits or fractures surfaces.

1.2 Super Duplex Stainless Steels

1.2.1 Stainless steel

For a steel to me known as a stainless steel is it required to have a Chromium content of 10.5% or greater. The Chromium content enables the material to form a passive Chromium Oxide layer on the surface, helping to prevent corrosion. Other alloying elements can be added to the steel to improve and adjust its properties, common additions are nickel, molybdenum, and nitrogen. (21)

316 / 316L are commonly used grades of stainless steel, they are an austenitic stainless steel which are non-magnetic. There are also ferritic and martensitic stainless steels. They type and grade of stainless steel is often selected based on the required materials properties associated with the specific grade. (21)

Duplex stainless steel has a alloying elements which enable the formation of both austinite and ferrite phases within it microstructure. Duplex stainless steel has better strength and corrosion performance when compared against more common 316L, this is however balanced by a generally high cost associated with Duplex material. (21)

1.2.2 Super Duplex Stainless Steel

Super duplex stainless steels (SDSS) are widely used in harsh environments due to their excellent corrosion resistance, high strength and good weldability. However they can form localised corrosion, namely pitting corrosion, in high temperature chloride containing environments. To improve the pitting corrosion resistance of SDSS, researchers and industry have developed alloys with different alloying elements, including copper and tungsten. (29)

1.2.3 Copper Additions:

There is discussion in industry and academia as to the effect of pitting corrosion resistance of stainless steels. Some sources suggest that copper addition improve corrosion resistance of SDSS's due to the novel Cu enriched on the surface. (30) (31)

However, some sources indicated that in passive regions Copper degrades the passive film due to an increase in the formation of Chromium enriched inclusions causing a decrease in corrosion resistance results in a lower Chromium concentration present in the passive layer. Some articles suggest that there is a possibility that Copper can degrade the stability of the protective layer by regions rich in Copper acting as preferential initiation site. (32) (33)

1.2.4 Tungsten Additions:

There is literature that suggests that tungsten can deliver a marked increase in the corrosion resistance of steel for both crevice and pitting corrosion. It is suggested that tungsten additions improve the re-passivation behaviour. There is limited data on this and no proposed mechanism as to how the presence of the additional tungsten improves the corrosion characteristics of the material. (34) (35) (36) (37) (38) (39)

1.2.5 Comparison of Duplex and Super Duplex Stainless Steels

Duplex stainless steels and super duplex stainless steels are both types of stainless steel alloys. They are both known for their excellent corrosion resistance and high strength. However they have some key differences that set them apart. (40) (41)

Duplex stainless steels are a combination of austenitic and ferritic stainless steels. They normally contain; 22-26% chromium, 4-7% nickel and 0.1-3% molybdenum.

Super duplex stainless steels, have a higher level of alloying elements. They normally contain; 24-26% chromium, 6-8% nickel, 3-5% molybdenum and 0.2-0.3% nitrogen. Some alloys have additional alloying elements such as copper and tungsten in relatively low levels. (40) (42)

Both duplex and super duplex stainless steels offer excellent corrosion resistance in various environments. However, super duplex stainless steels are known to have higher resistance to corrosion in more aggressive environments, such as those containing chlorides and acid. (43)

Super duplex stainless steels are generally stronger than duplex stainless steels due to their higher levels of alloying elements, particularly nitrogen. This makes super duplex stainless steels more suitable for applications that require high strength and durability. (43)

Super duplex stainless steels are generally more expensive than duplex stainless steels due to their higher alloying content and more complex manufacturing processes, resulting from their higher strength and hardness. This means that SDSS are normally only used in situations where high component cost can be justified, in critical components or systems that are hard to inspect and maintain.

Duplex stainless steels are generally easier to weld than super duplex stainless steels. Super duplex stainless steels require more care and attention during the welding process to prevent issues such as cracking and lack of fusion. (44) (40) (45)

1.3 Previous work on the effect of copper and tungsten addition on the pitting corrosion resistance of SDSS.

Previous investigations looked at the behaviour of SDSS when undergoing potentiodynamic polarisation, by steadily increasing the polarisation of the material under test until the sample begins to corrode as a constant temperature. From this testing little conclusive differences and effects were measured between alloys with copper and tungsten vs those without. Further to this

previous testing has struggled to promote pitting corrosion, instead producing preferential phase corrosion mechanisms. (46)

Building on the previous work conducted on this topic it was decided to find a reproduceable method to promote the pitting corrosion mechanism in the SDSSs to enable investigation into their pitting corrosion resistance, and the effect there in, of copper and tungsten addition. Following initial investigation and testing it was found that a critical pitting temperature test resulted in the repeatable production of pits in all the SDSS alloys under test. This method was then taken forward as the primary form of investigation for this project.

2.0 Experimental Methods

The work carried out during this research involves the testing of SDSS to assess their critical pitting behaviour. This section outlines the materials and chemicals used alongside the experimental procedures followed.

2.1 Materials

Langley Alloys Ltd. supplied three grades of Super Duplex Stainless Steel (SDSS); Ferralium 255 (UNS S32550), Zeron 100 (UNS S32760), SAF2507 (UNS S32750). The composition of each alloy (seen in **Table 2.1**) are very similar for elements other than Copper (Cu) and Tungsten (W), meaning difference in the corrosion behaviour between the three samples can be concluded to be due to the variations in the Cu and W composition of the samples. It is therefore of interest to determine whether changes in these elements influence corrosion performance.

Table 2.1: Chemical composition of the Super Duplex Stainless Steels samples (wt. %)

	Cr	**Ni**	**Mo**	**Cu**	**W**
Ferralium	24.5 - 26.5	5.5 - 6.5	3.1 - 3.8	1.5 - 2.0	-
Zeron	24.0 - 26.0	6.0 - 8.0	3.0 - 5.0	0.5 - 1.0	0.5 - 1.0
SAF	24.0 - 26.0	6.0 - 8.0	3.0 - 5.0	< 0.5	-

The materials have comparable microstructures, made up of Austinite grains and Ferrite a matrix. Previous investigations revealed the microstructure of the SDSS materials through electrochemical etching by polarising the samples to

1.25 V vs SHE in 0.6M NaCl solution at pH 5.7 until the microstructure was visible. A comparison of the materials can be seen below in **Figure 2.1**. (46)

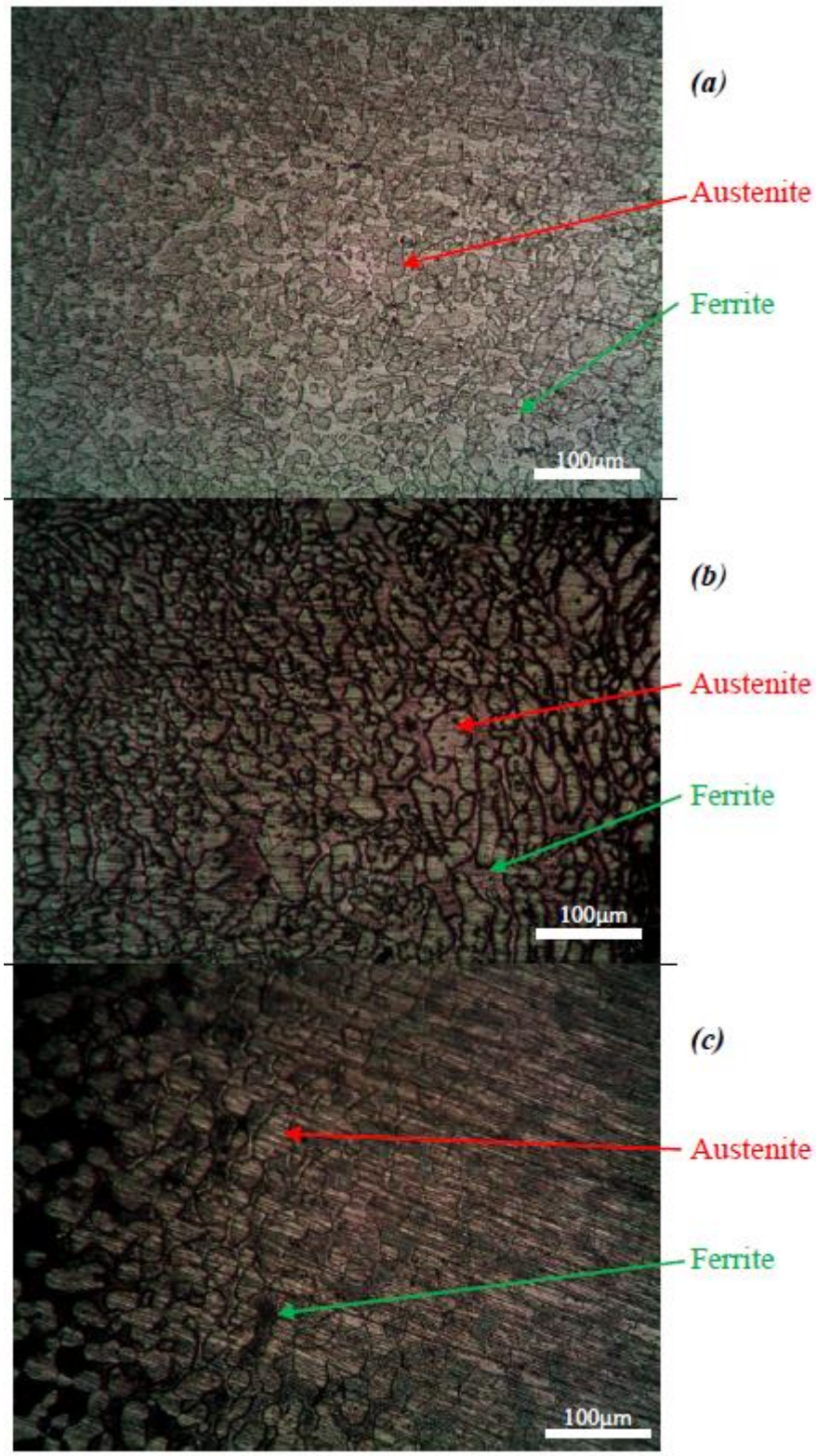

Figure 2.1: Microstructure comparison of the SDSS materials. (a) Ferralium, (b) Zeron, and (c) SAF. (46)

2.2 Sample Preparation

SDSS samples were cut into rods with 12.7mm diameter. The samples were ground using European P-grade Silicon Carbide abrasive paper with varying levels of grit paper depending on the test being conducted. Before each experiment, samples were degreased and rinsed with ethanol and distilled water.

2.3 Critical Pitting Temperature Experiments

The experimental method and equipment set up was consistent throughout the CPT experimentations, with some minor adjustments relevant to the specific test. The method was iteratively refined and tested which resulted in a reliable and effective test protocol. Below is the methodology that was developed and implemented in the CPT experiments.

Potentiostatic polarisation measurements were recorded using a Solartron 1280 Electrochemical Measurement Device. Potentiostatic polarisation consists of holding the material under test and a constant potential throughout the testing. Samples were held at a 0.9 Volts vs the saturated calomel electrode (SCE) reference electrode. Samples were polarised to 0.9 Volts to be a fraction below the polarisation at which the SDSS's would break down, this was found in previous potentiodynamic investigations (46). The OCPs of all the materials under test was found to be -0.05 Volts at 70°C ±0.01. The 5% NaCl electrolyte was heated using a EchoTherm HP60-2 hot plate. (23) The tests were conducted using a three electrode step up, consisting of; the SCE as a reference electrode, the sample being the test electrode and a platinum counter electrode. A temperature ramp rate of 0.5 ^{O}C/min was selected due to the high repeatability at this setting with the equipment and it enabled high granularity of temperature increase vs current density. The rate of increase of the temperature and the measured temperature were controlled and measured by the thermocouple, shown in **Figure 2.2**. The initial electrolyte temperature was selected to be 70 ^{O}C as none of the alloys were found in initial testing to break down at this

temperature whilst being polarised to 0.9 Volts, with the applied polarisation. However, 70 ^{O}C is suitably close to the alloys CPT that test duration was reduced to a minimum. The electrolyte was deoxygenated to reduce the chance of repassivation of the passive layer or of formed pits, by reducing the oxygen concentration in the solution it is less likely that the Chromium in the material can react with it, repassivating the surface. In order to deoxygenate the solution, it was sparged by bubbling nitrogen gas through the solution for 20 minutes prior to testing with the beaker being loosely sealed with Parafilm. During the test a nitrogen rich atmosphere was maintained in the headspace of the beaker to prevent oxygen from the sounding air redissolving into the solution. This was done to reduce the available oxygen in the solution for the chromium to use to reproduce the passive layer, reducing the chance of re-passivation of any formed pits. The sample was electrically connected as the working electrode using a jubilee clip and placed into the solution as seen in **Figure 2.2**. After film breakdown / corrosion initiation was measured, by an increase in the current density, the experiment was permitted to run for a further 6 minutes to allow for the pits to develop. Because the rate of increase of the temperature was constant, the current density can be plotted directly against the temperature solution as time in seconds is a common measurement output of both variables.

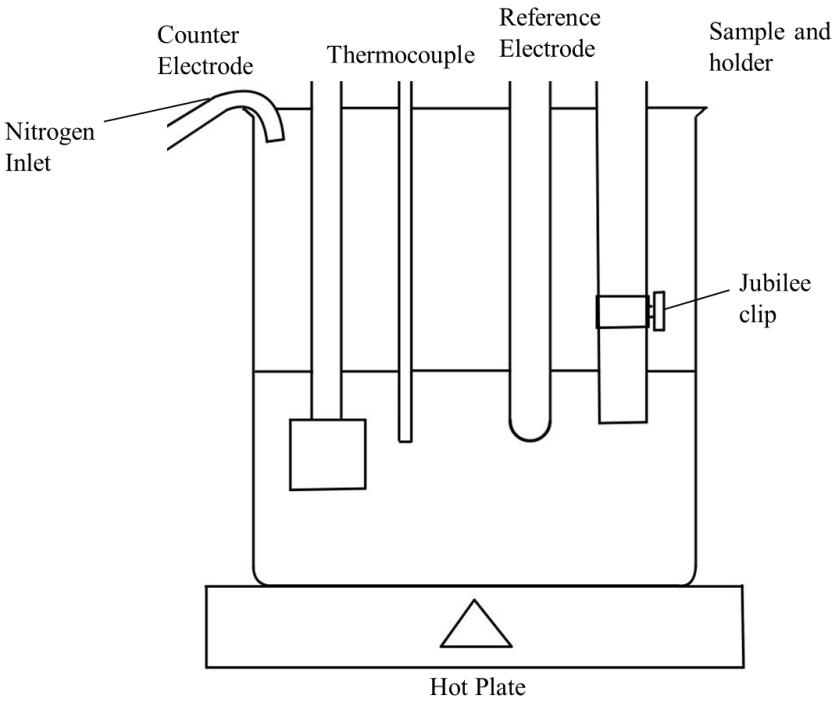

Figure 2.2: Schematic Representation of CPT apparatus set up.

2.3.1 Surface Roughness Experiments testing in order to determine its effect on measured CPT

Three Ferralium sample were prepared to differing surface roughness's. In all cases the circular sides of the rod were prepared with 4000g to ensure a consistent surface finish across the samples. Following this the face of each rod was prepared with different grade of paper by grinding the face with the respective sanding paper, (400g 1200g and 4000g). Each sample was inspected using optical microscopy to ensure that the surface finish resulting from the sand paper was uniform throughout the face of the material.

Images were obtained before and after testing, to help evaluate the effect of the surface finish on the pits that formed. Samples were immersed in 3.5% NaCl solution.

2.3.2 The effect on breakdown time on the pit formation and density in critical pitting temperature sweeps.

An investigation was conducted to find the optimum time after breakdown to allow the alloys to run in their CPT sweeps, to allow for proper formation of pits and increase the density of the formed pits to a reliable level. If the sample was stopped as soon as the measured current density increased, above a near zero value, then little to no pits could be imaged and assessed. To find the optimum time after breakdown had occurred 3 sweeps were conducted allowing for a post breakdown time of 1, 3 and 6 minutes respectively. After the sweep was complete the samples were imaged with SEM to assess the number of measurable pits. The time that produced a reliable number of well-formed pits was used in the further testing of the CPT in the SDSS alloys.

2.3.2 The effect of pH on critical pitting temperatures of SDSS's

All pH measurements were conducted with a calibrated pH meter immediately prior to testing. Acid solutions were adjusted to pH 4 using dilute HCl. Alkaline solutions of both pH 7 and pH 10 were made using dilute NaOH. Each alloy was tested at 4, 7 and 10 pH respectively with an additional repeat test for every alloy at every pH (totalling 18 sweeps).

2.4 Scanning Electron Microscope Imaging

A scanning electron microscope (SEM) produces images by scanning the surface of conductive samples with a high energy beam of electrons and capturing the reflected and scattered electrons. Depending on the manner of the interaction of the electron with the material, different information is provided in the image. Secondary electrons provided high topographical (surface) information. Whereas backscatter electrons provided contrast between atomic masses present in the material. This method results in the ability to image with a high depth of field and resolve features in the range of a nanometre.

SEM images were obtained using a Zeiss Evo LS25 SEM. All samples were cleaned with ethanol to remove any surface contaminants, and then mounted

using conductive carbon tape which ensured a strong electrical connection prior to imaging.

2.5 Image Analysis

ImageJ software was used to measure the surface area and number of the pits in images obtained by the SEM. Images were taken of every visible pit on every sample. The images were then loaded into the ImageJ software. The scale bar in each image was used to calibrate the respective images to enable comparison between the gathered data. A measurement was taken around the circumference of the pit to find the total area of the pit, which was repeated three times to find an average value for each pit. The repeat was conducted to reduce the error produced by the manual drawing of the circumference. **Figure 2.3** shows an example pit with the outline drawn around the affected area.

Data from the image analysis was compiled to assess the effect of pH on the average size of the formed pit. The total pitted area of the samples surface was also calculated and compared to show the effect of pH.

A limitation of this method is that there is not information on the total depth or volume of the pit. This information is not possible to gather through SEM imaging alone in a reliable manner. Volume measurements through SEM in this case are hindered by the presence of a pit cap, obscuring imaging of the internals of the pit. Comparative mass measurements could be conducted, however the mass loss from the pits is very small and would require a balance with high accuracy.

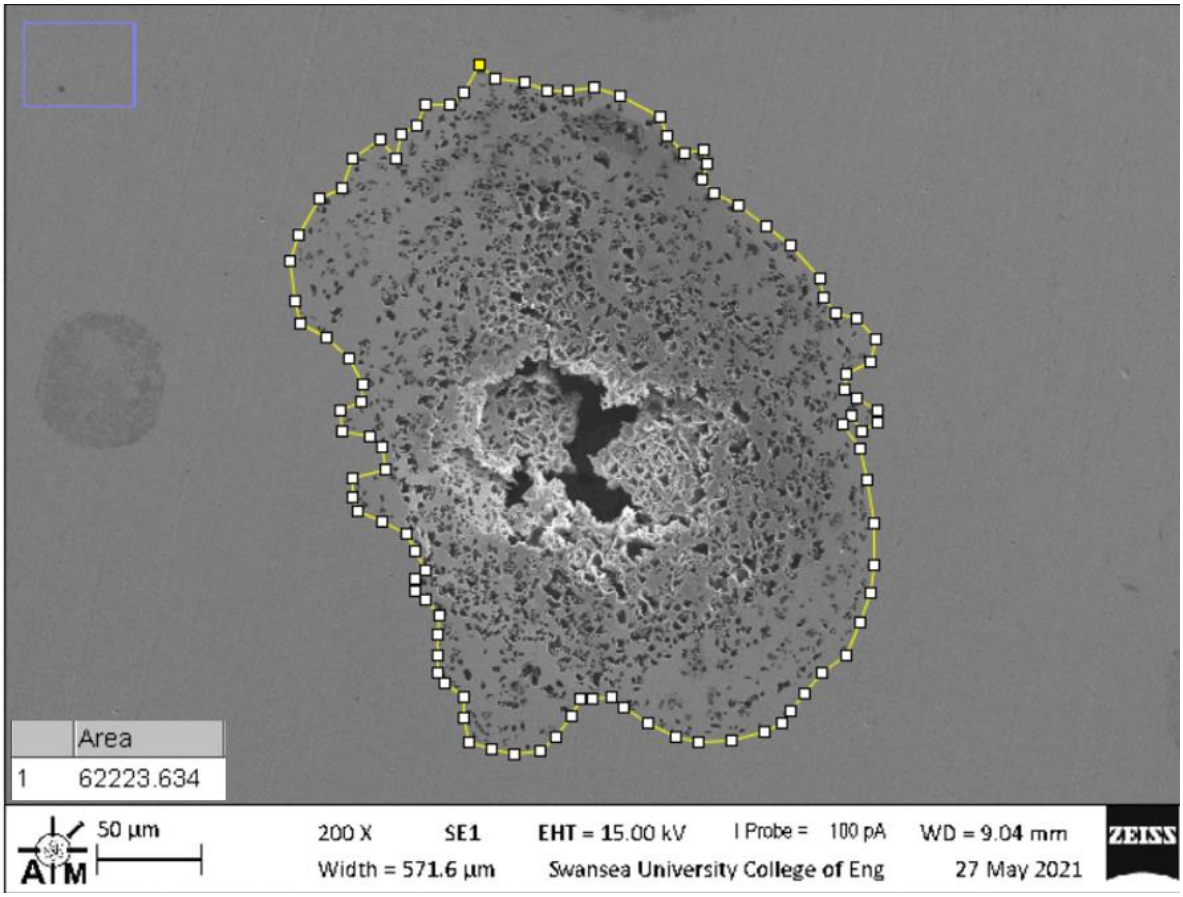

Figure 2.3: ImageJ processing of SEM image to find the total average area of the pit formed in SDSS during CPT testing.

2.7 Time Lapse Imaging of CPT

Time-lapse optical microscopy involves capturing a micrograph of the samples surface at constant intervals in time a Meiji MT8000 microscope was used in an unsubmerged configuration. To prevent the water vapour clouding the lens, a fan was used to demist the surface. This enabled the progress of a developing corrosion system, like those occurring during a CPT breakdown, to be observed.

The general system for the polarisation and experimental set was up the same as previously stated in the pH assessments. The key difference from the TLI experimental setup and the pH CPT setup is that the specimen must be inverted so that its flat face is in the uppermost direction. With the specimen in the upward direction, it is possible to use a microscope to capture an image of the corrosion surface whilst it is undergoing potentiostatic polarisation.

The way the samples were prepared and electrically connected to the test was changed from that of the pH CPT experimental setup in order to enable the time lapse imaging. Short rod samples were ground with 4000g sanding paper, and an insulated copper wire was soldered to their base. The rod and wire were then wrapped in rubberised tape which both insulated the electrical connection from the electrolyte and ensured that only the flat surface being monitored by the time lapse imaging was exposed, schematic of the set up can be seen in **Figure 2.4**. A repeat was conducted for each alloy.

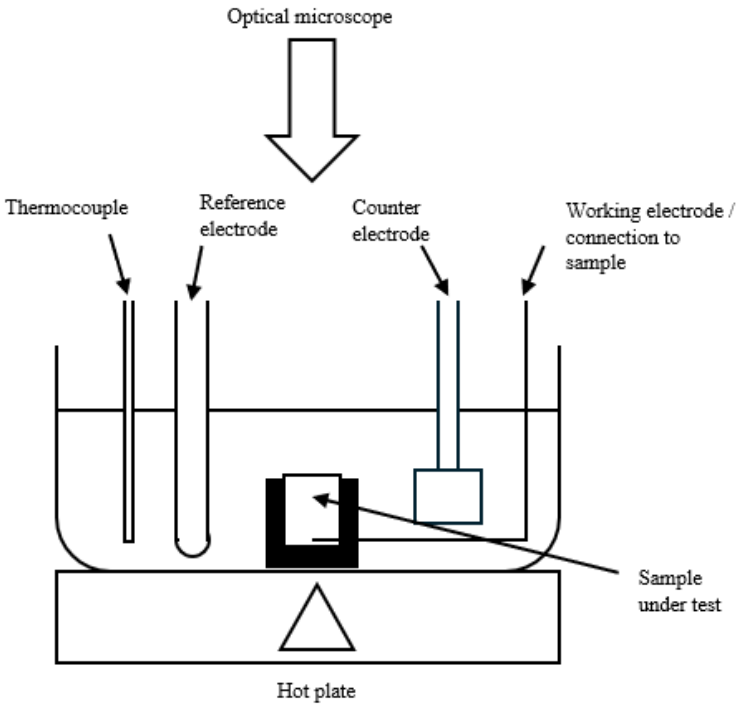

Figure 2.4: Schematic Representation of TLI CPT apparatus set up.

3.0 Results

3.1 Critical Pitting Temperature measurements

For the CPT tests the results have been plotted on graphs. The graphs have the temperature on the x axis and the measured current density on the y axis. Depending on the test the sweeps have been grouped on certain graphs to display how their response compares to other test samples.

Initially a series of tests were conducted to refine the methodology of the CPT test set up. Once the methodology was successfully refined it was leveraged to investigate the effect of the surface roughness of the material on the CPT.

3.1.1 Assessment of the samples surface roughness on their CPT

Ferralium was selected for this test as it was deemed that only one material needed to be tested. An assumption was made that the effect of the surface roughness would reasonably consistent between the different materials under test. Ferralium was selected as initial testing showed that it had the lowest CPT and therefore would be easier test due to the reduced heating of the solution required. A range of 3 surface finishes were selected as being attainable through manual manufacturing. These namely being the surface texture produced by 400, 1200 and 4000 grit sandpaper. (P400g, P1200g and P4000g)

The test was carried out as it was hypothesised that rougher surfaces would have a detrimental effect on the CPT caused by possible increase in local concentrations of ions in the crevice-like features or scratches formed in the material by the sanding paper. Additionally, a scratch or rougher surface could make the initiation of a pit thermodynamically more likely due to an increase likelihood of crevice corrosion occurring. (47)

Following the Ferralium samples preparation, the samples of varying roughness were subjected to a Critical Pitting Temperature sweep. The Potentiostatic graphs can been seen below in **Figure 3.1**.

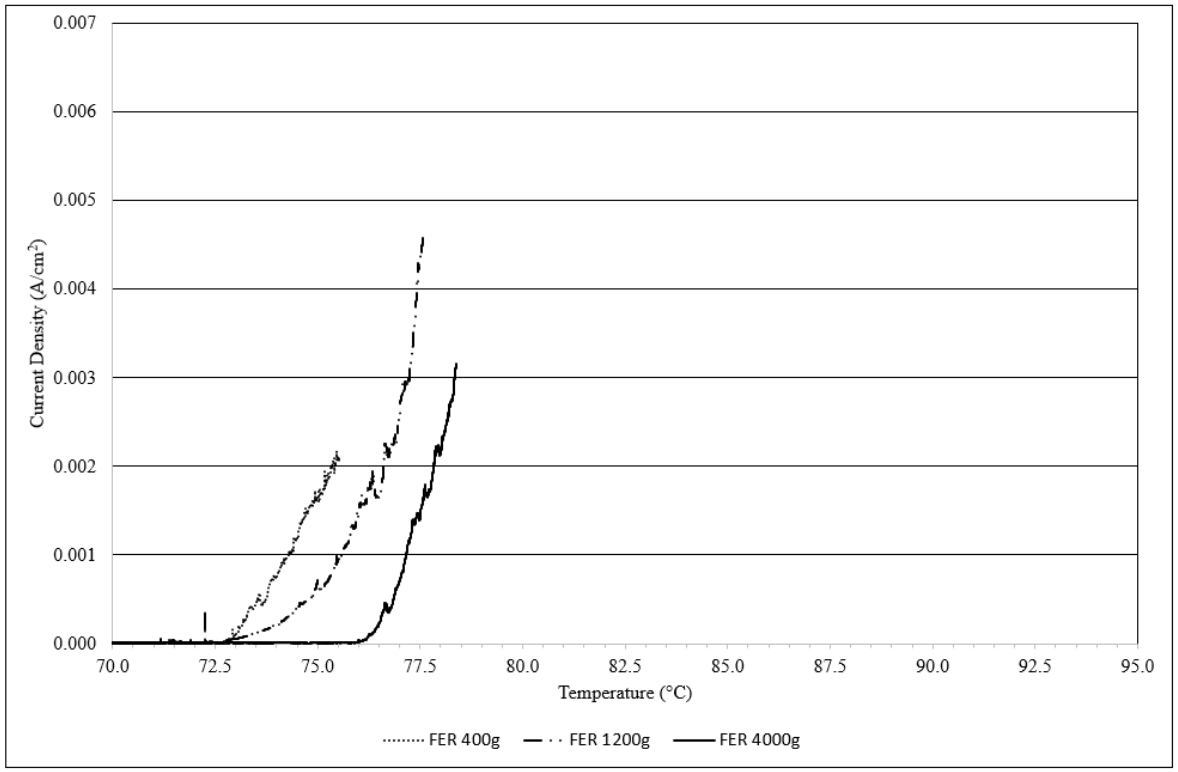

Figure 3.1: A graph showing the potentiostatic sweeps performed on Ferralium samples with surface finshes produced by sanding paper of 400g, 1200g, and 4000g.

The sample with the roughest surface finish, the 400g sample, started to corrode at 73.0 ^{o}C. The sample with the smoothest surface finish started to corrode at 76 ^{o}C. 4000g surface finish was selected as the preparation method for the further pH CPT investigation due to its increased resistance to CPT and potential reduction in crevice corrosion-like effects. The different surface finishes of the samples undergoing the CPT sweeps can be seen in **Figure 3.2**. In this comparison the apparent size and depth of the scratch lines reduce with the increasing grit (g) value. Following the experiment, pits were imaged using SEM to determine whether the surface finish affected the shape and apparent mechanism of pit formation and propagation. A comparison in **Figure 3.2** does

not present any notable differences in pit appearance. They have very similar lacy cap formations covering the pits. It is potentially notable that as the surface roughness of the sample decreases the size of the pit increases. However, there is an insufficient data set to draw any meaningful conclusions from this, with only test run of each surface roughness. Also for this investigation there was not an extensive study conducted on every pit formed on each sample, for a more valid conclusion to be formed this test would need to be repeated with imaging of every formed pit.

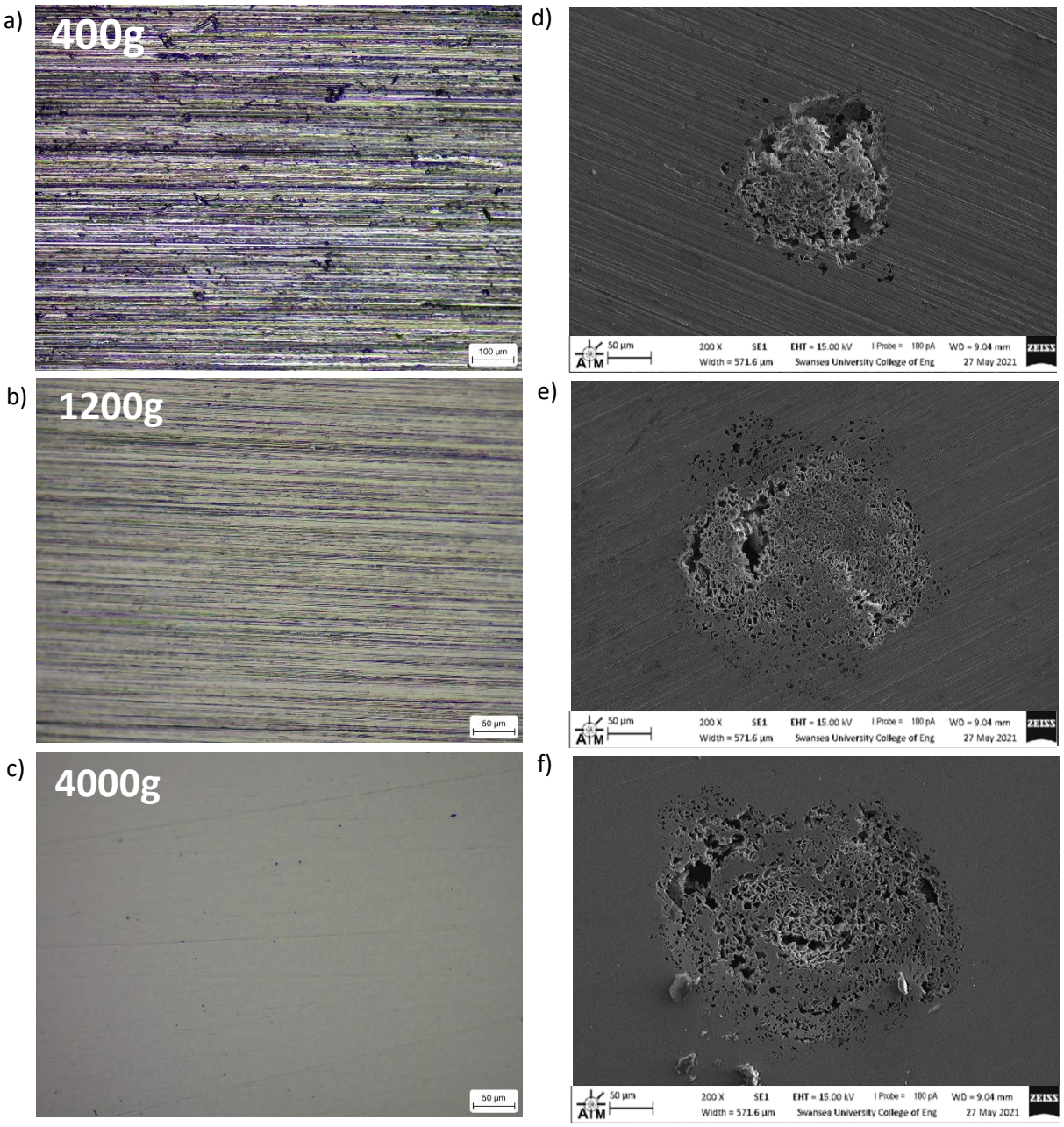

Figure 3.2: a) b) c) Optical image of scratch pattern prior to CPT testing at P400, P1200, P4000 grit respectively. d) e) f) SEM image of pits formed after CPT testing at P400, P1200, P4000 respectively.

3.1.2 Assessment of optimum breakdown time for further CPT experimentation

The measurements taken during the critical pitting investigations allow for identification of the breakdown temperature through noting where the measured current density forms a spike or a peak. If the test is not continued for sufficiently long period after the passive layer of the material has broken down, then there is not enough time for the corrosion cells to grow and undergo the formation of a pit. A test was conducted to find the optimum time to allow the test to run for after a measured breakdown, to ensure the production of enough pits to get a statistically reliable number and size of pits and that also produced a clear critical pitting temperature. Samples were polarised for 3 different times after a visible breakdown in the passive layer was measured; 1, 3 and 6 minutes. The results are shown in **Figure 3.3**.

The results of this investigation showed that a breakdown in the protective film,

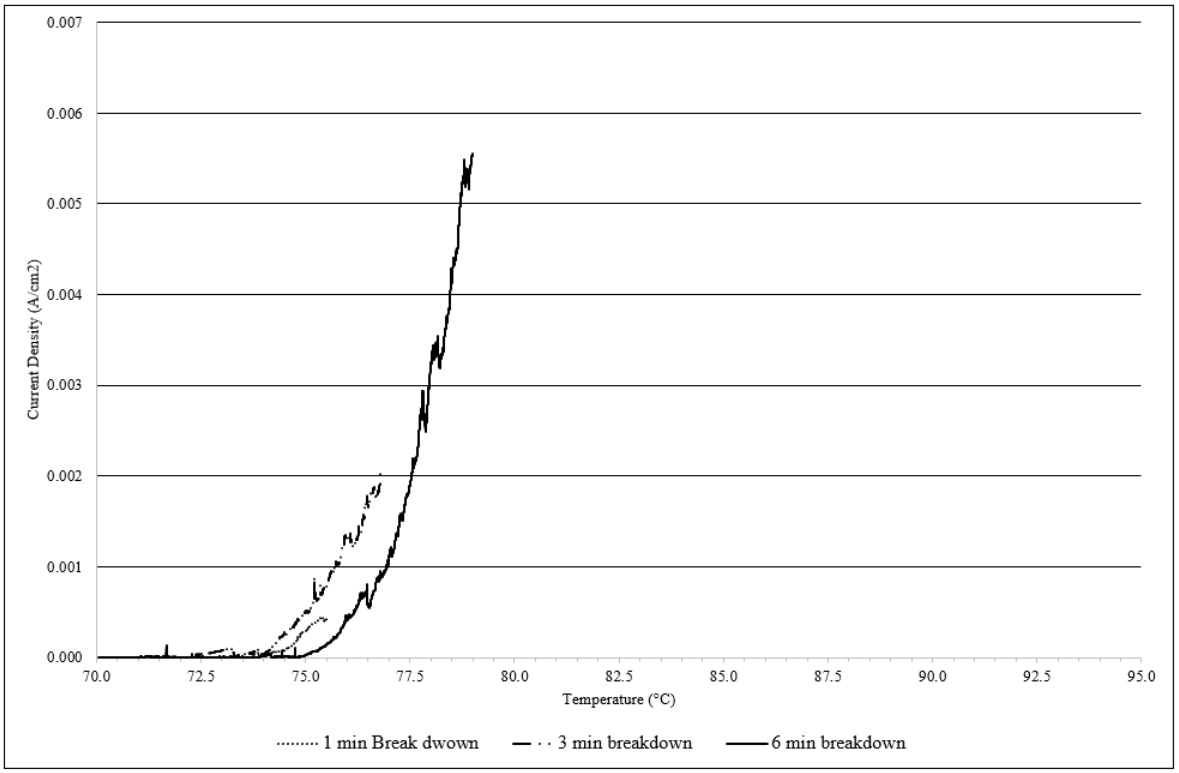

Figure 3.3: A graph showing the potentiostatic sweeps performed on Ferralium samples with different breakdown times; 1 minute, 3 minutes,6 minutes.

leading to an increase in the measured current density was easily and repeatably measurable. This was consistent throughout the tested breakdown times, with

the 1 minute break down time, (a), being the smallest peak and 6 minutes (c) being the largest, as seen in **Figure 3.3**. However, there were no visible pits on the sample left to break down for 1 min after the breakdown of the passive layer was measured. For the sample that was left for 3 minutes only 1 pit was found through SEM analysis. The 6 minutes sample had a much larger data set of pits to be analysed. Due to the larger number of pits and more developed pits it was concluded that a breakdown time of 6 minutes should be selected as the most reliable breakdown time for the proceeding CPT investigation into the effect of pH.

3.1.3 Effect of pH on critical pitting temperature resistance of SDSS

Figure 3.4 shows all the sweeps that were produced in the pH CPT testing compiled into one graph to show trends. Three distinct groups are visible in **Figure 3.4**, each respective alloy has formed a group with no overlap from other fellow CPT peaks. For clarity the graphs have been separated into pH specific graphs (**Figures 3.5 – 3.7**) and material specific (**Figures 3.8 – 3.10**).

Figure 3.5 shows the tests sweeps collected for Ferralium, Zeron and SAF from a 4pH CPT test, with two sweeps for each material. There is a grouping of the CPT results which align with the respective materials. Ferralium material breaks down at approximately 75^{o}C. Zeron at approximately 83^{o}C and SAF at approximately 88^{o}C.

Figure 3.6 shows the tests sweeps collected for Ferralium, Zeron and SAF from a 7pH CPT test, with two sweeps for each material. There is a grouping of the CPT results which align with the respective materials. Ferralium material breaks down at approximately 74^{o}C. Zeron at approximately 85^{o}C and SAF at approximately 88^{o}C.

Figure 3.7 shows the tests sweeps collected for Ferralium, Zeron and SAF from a 10pH CPT test, with two sweeps for each material. There is a grouping of the CPT results which align with the respective materials. Ferralium material breaks

down at approximately 74°C. Zeron at approximately 84°C and SAF at approximately 89°C.

Figure 3.8 shows the Ferralium sweeps collected at 4pH, 7 pH and 10pH. All sweeps have a tightly grouped breakdown temperature of approximately 75 °C.

Figure 3.9 shows the Zeron sweeps collected at 4pH, 7 pH and 10pH. All sweeps have a tightly grouped breakdown temperature of approximately 84 °C.

Figure 3.10 shows the SAF sweeps collected at 4pH, 7 pH and 10pH. All sweeps have a tightly grouped breakdown temperature of approximately 87 °C.

From these results a clear grouping of each material type can be seen, with Ferralium having a lower CPT than Zeron and SAF. SAF has on average the highest measured CPT compared to Zeron and Ferralium. Further to this, negligible difference in CPT can be seen caused by changing the pH of the solution with each of the alloys.

One of the trends in the data presented in **Figure 3.4** is that there are some similarities with the size and shape of the peaks formed relating to the different alloys. Ferralium and SAF peaks tended to be taller than Zeron peaks.

Figure 3.11 shows CPT plotted as a function of pH. The interpretation of the CPT is open to being influenced by human error, this is because some of the sweeps have an unclear start to the breakdown. To reduce the influence of the human error an offset measurement was also implemented to improve the reliability of the CPT reading. The offset was set at 0.001 A/cm^2 of the sweeps current density. **Figure 3.12** shows the plot of the 0.001 offset CPT measurement. The offset method used presents an increase in the linearity of the measured CPT of each sample. In **Figure 3.12** very little deviation in the alloys measured CPT values depending on the changing pH can be seen.

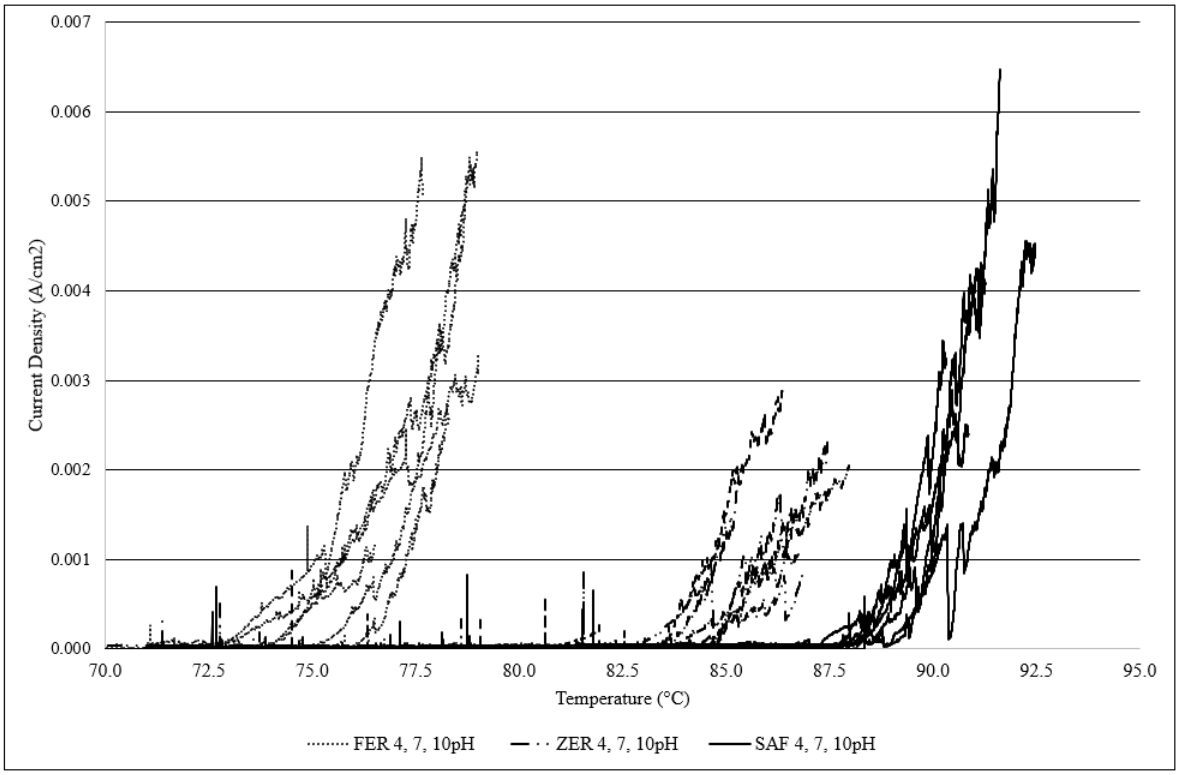

Figure 3.4: A graph showing the potentiostatic CPT sweeps conducted on Ferralium, Zeron and SAF samples at 4, 7 and 10 pH .

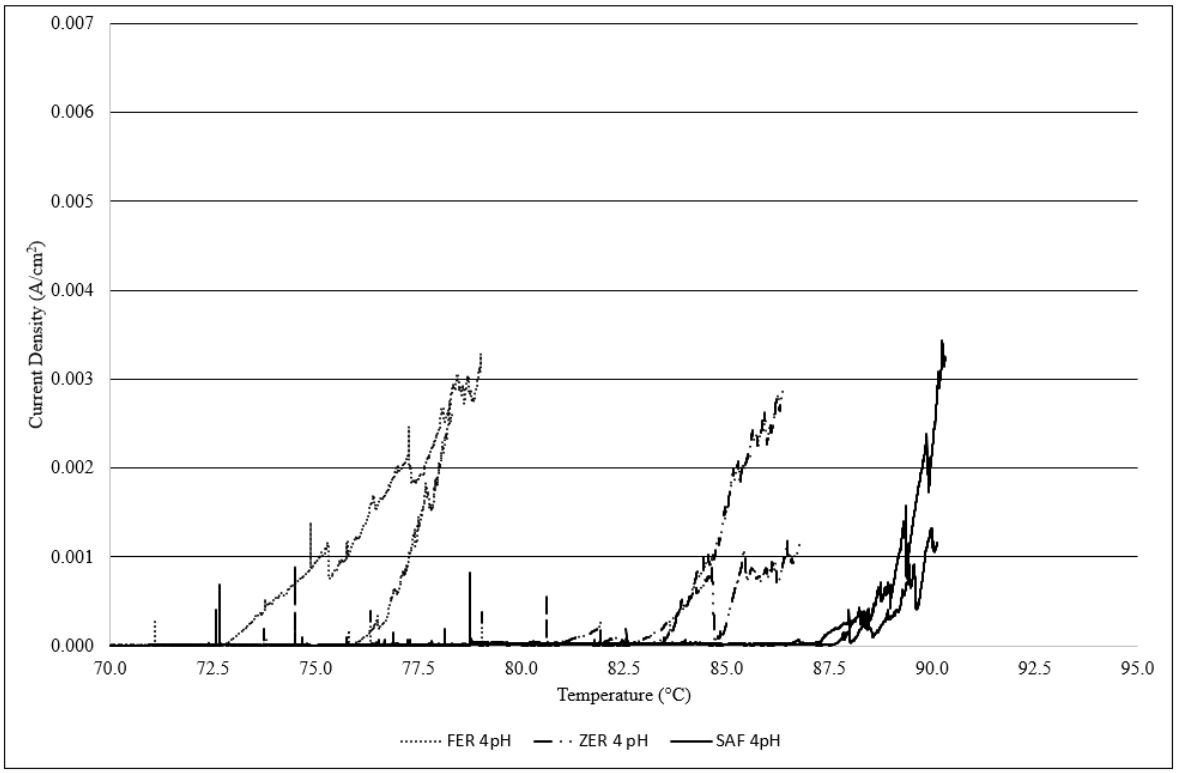

Figure 3.5: A graph showing the potentiostatic CPT sweeps conducted on Ferralium, Zeron and SAF samples at 4pH.

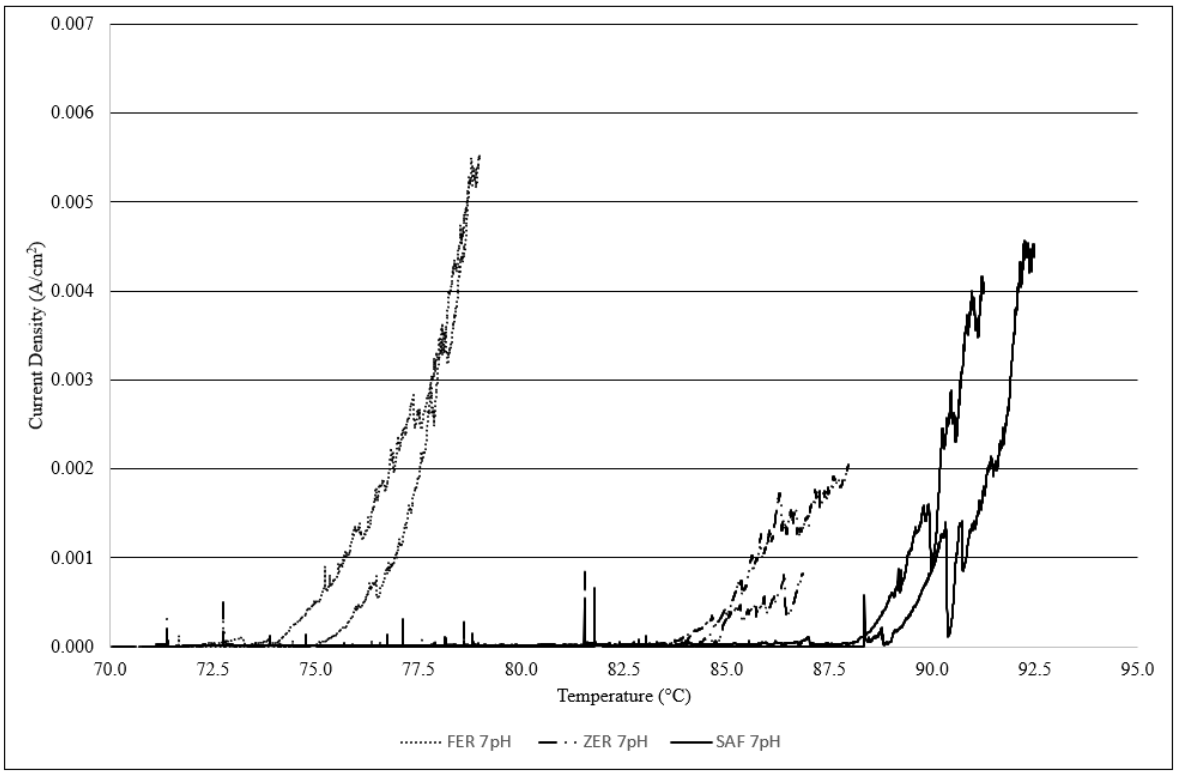

Figure 3.6: A graph showing the potentiostatic CPT sweeps conducted on Ferralium, Zeron and SAF samples at 7pH.

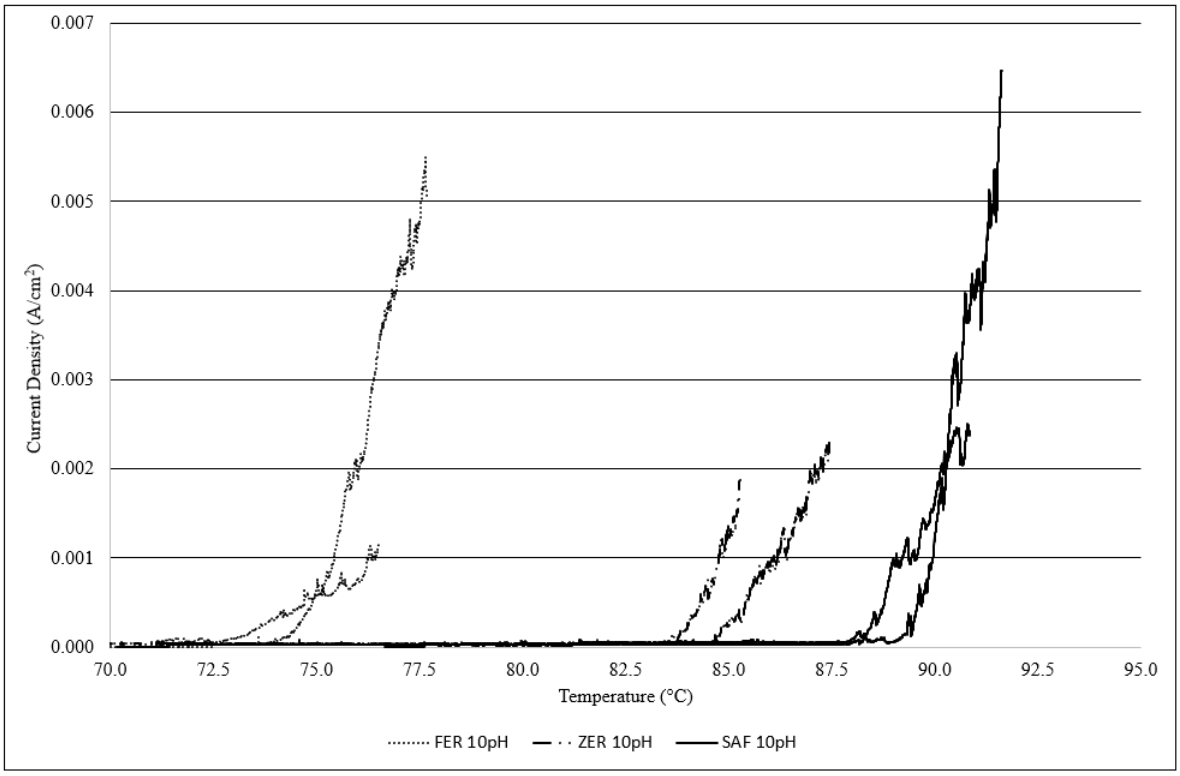

Figure 3.7: A graph showing the potentiostatic CPT sweeps conducted on Ferralium, Zeron and SAF samples at 10 pH.

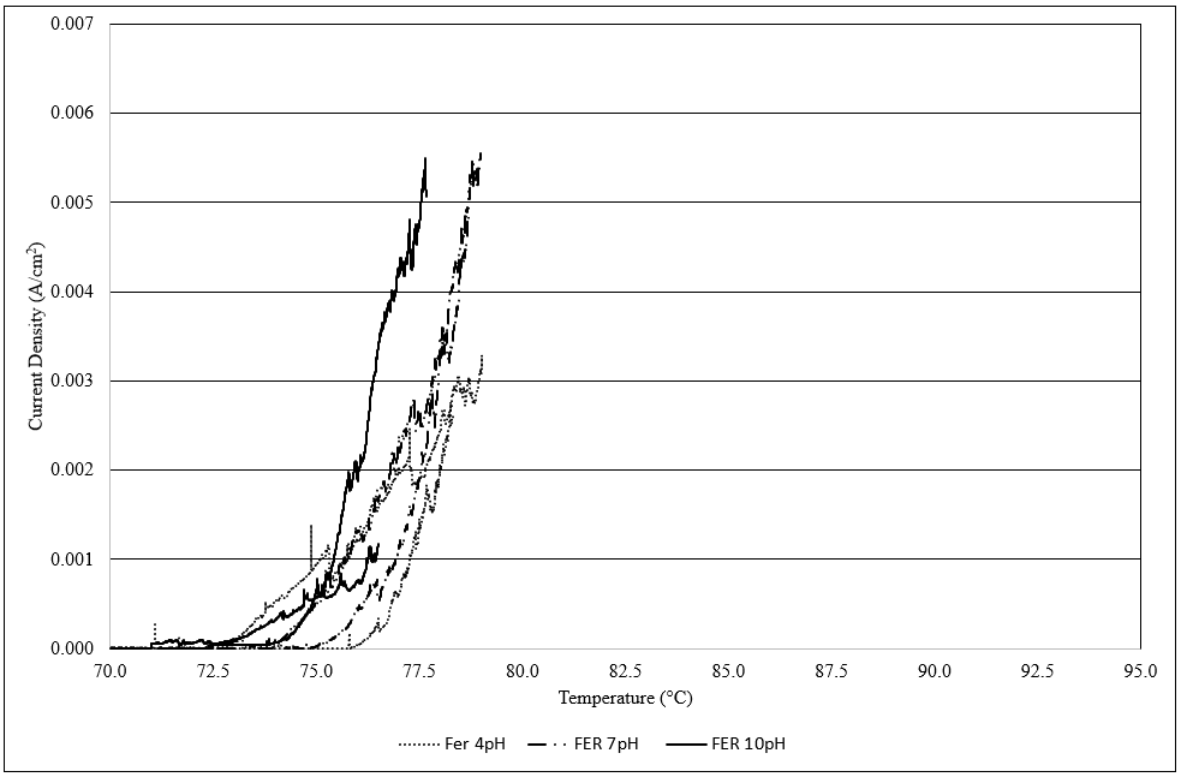

Figure 3.8: A graph showing the potentiostatic CPT sweeps conducted on Ferralium at 4, 7 and 10 pH

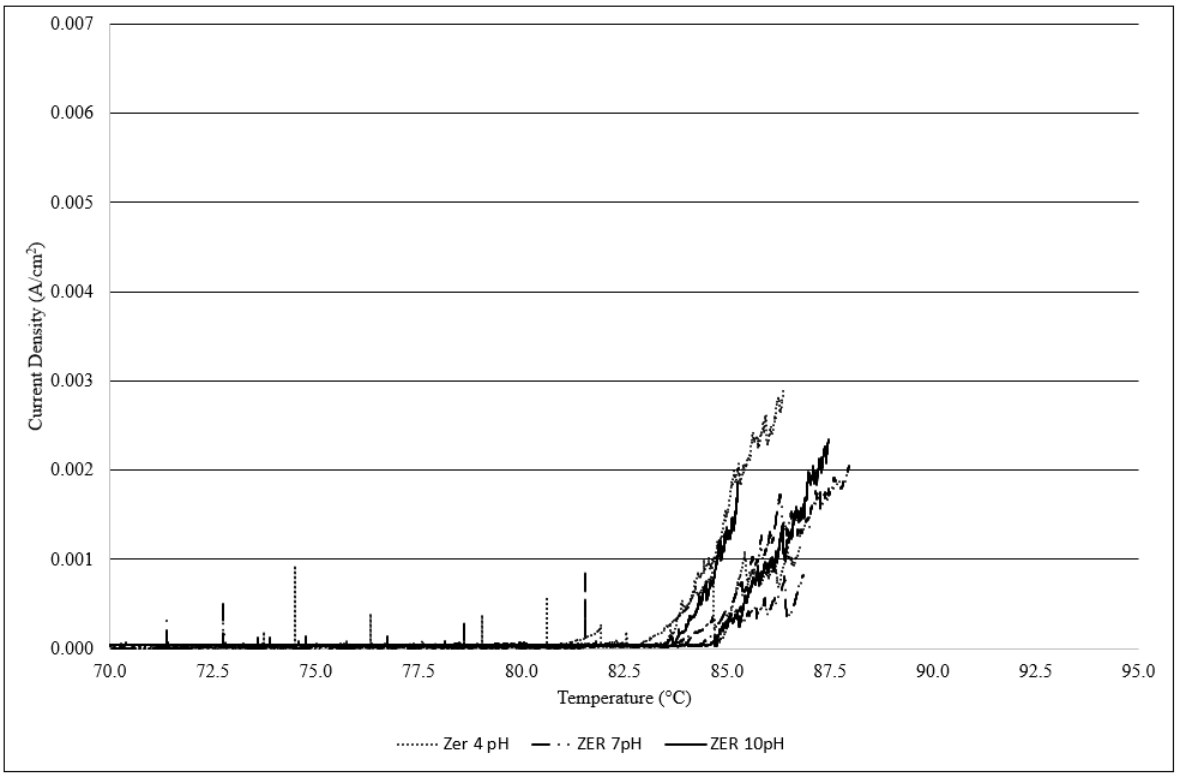

Figure 3.9: A graph showing the potentiostatic CPT sweeps conducted on Zeron at 4, 7 and 10 pH.

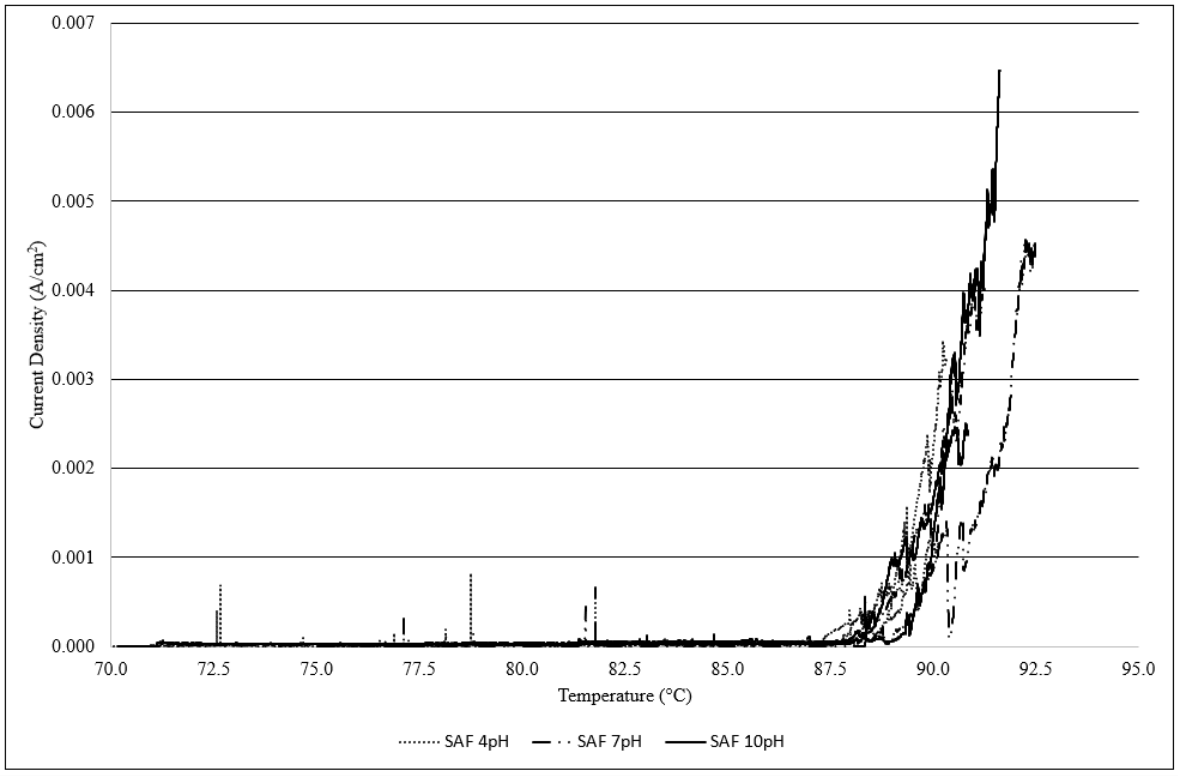

Figure 3.10: A graph showing the potentiostatic CPT sweeps conducted on Zeron at 4, 7 and 10 pH.

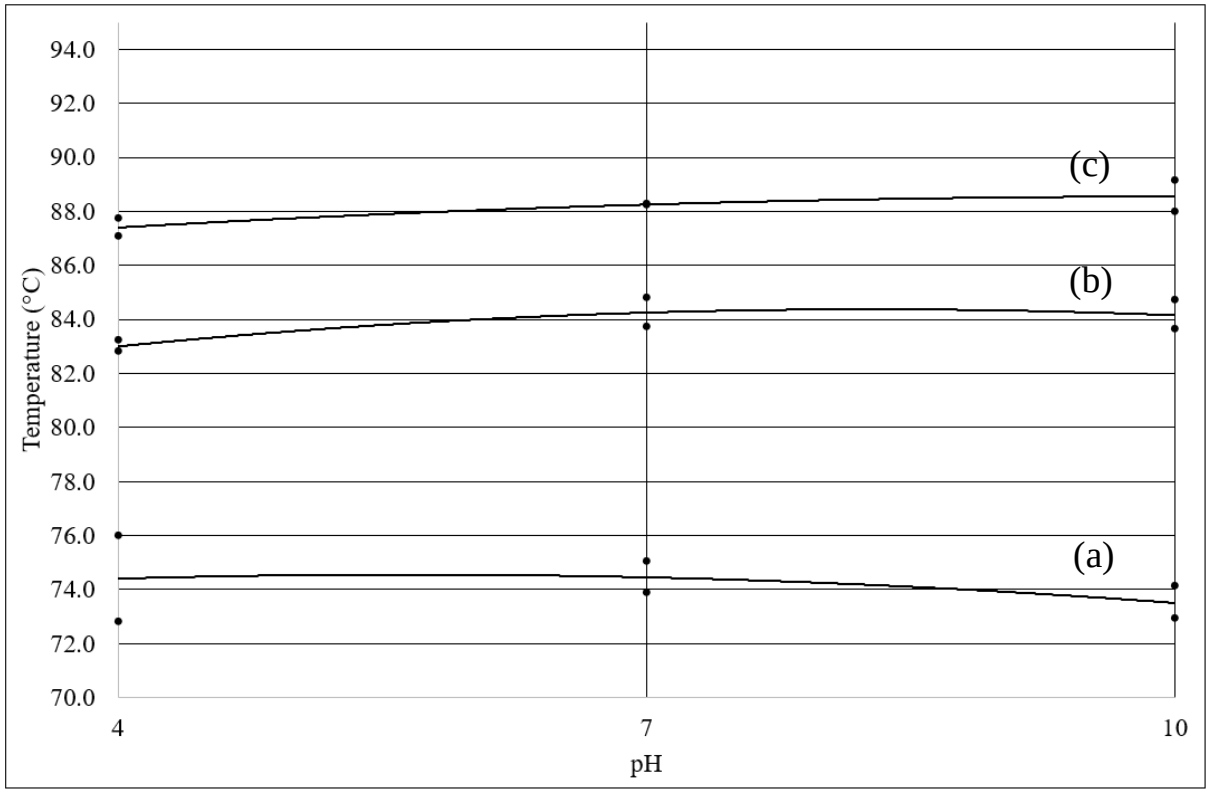

Figure 3.11: A graph showing the CPT values measured for Ferralium (a), Zeron (b) and SAF (c) samples at 4, 7 and 10 pH.

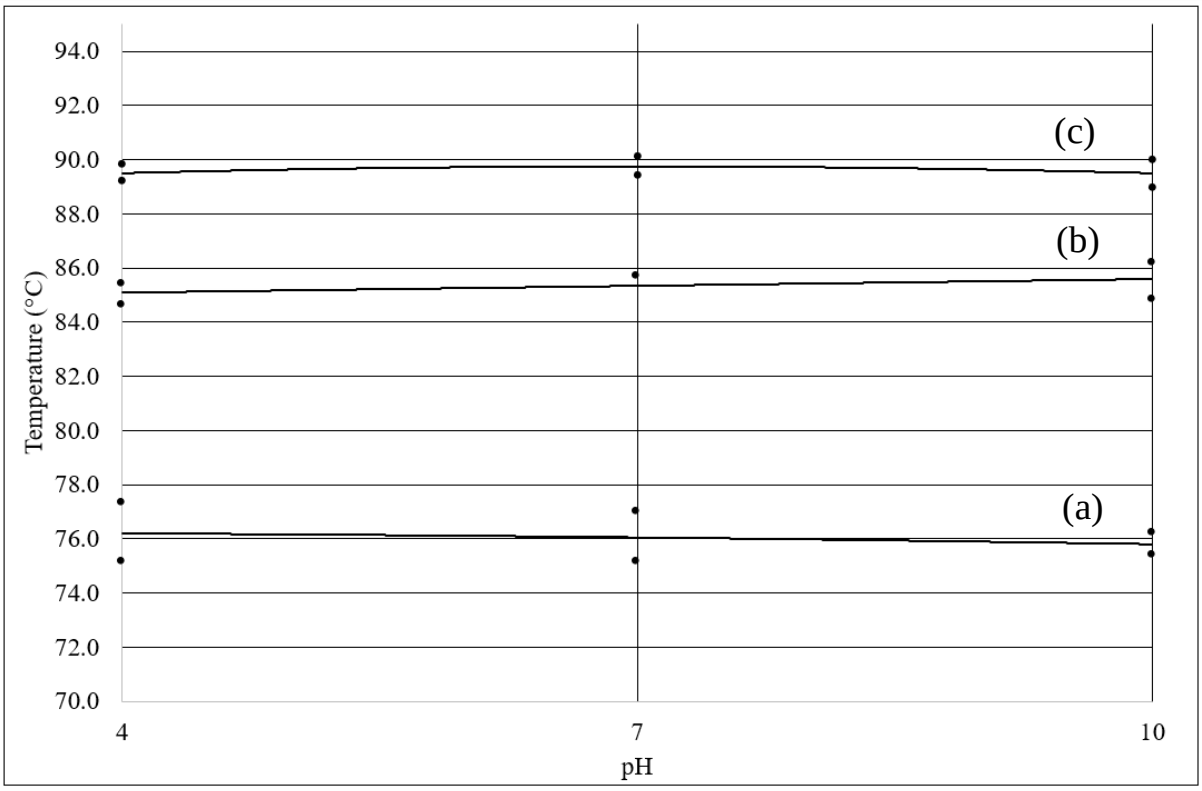

Figure 3.12: A graph showing the 0.001A/cm^2 offset CPT values measured for Ferralium (a), Zeron (b) and SAF (c) samples at 4, 7 and 10 pH.

3.2 Pit Size Analysis

3.2.1 Effect of pH

3.2.1.1 Average pit size

The results of the average pit size results are presented in **Figure 3.13**. Pits of larger area can be seen to have formed on samples immersed in pH 7 electrolyte compared to 4 and 10 pH. Ferralium samples appear to form the largest pits with SAF forming the smallest.

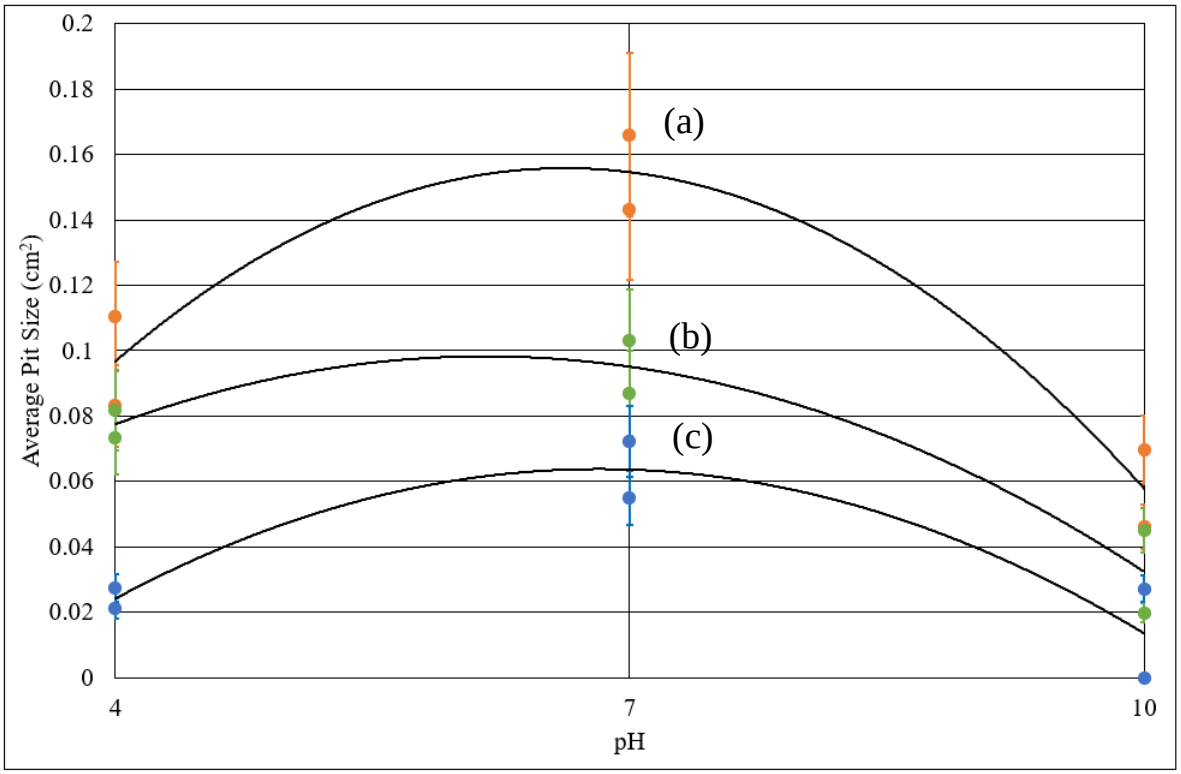

Figure 3.13: A graph showing average measured pit size for Ferralium (a), Zeron (b) and SAF (c) samples at 4, 7 and 10 pH.

3.2.1.2 Total pit area

The results of the total measured pit size are shown in **Figure 3.14.** A very similar trend to that stated above is present however at pH 10 it appears that Ferralium has produced the smallest total area of pit on the surface. There is a limitation in this test as it does not capture any pits that may have formed on the

edges of the sample, however this was observed as being constant across all the samples and can be used as a comparison between the different alloys.

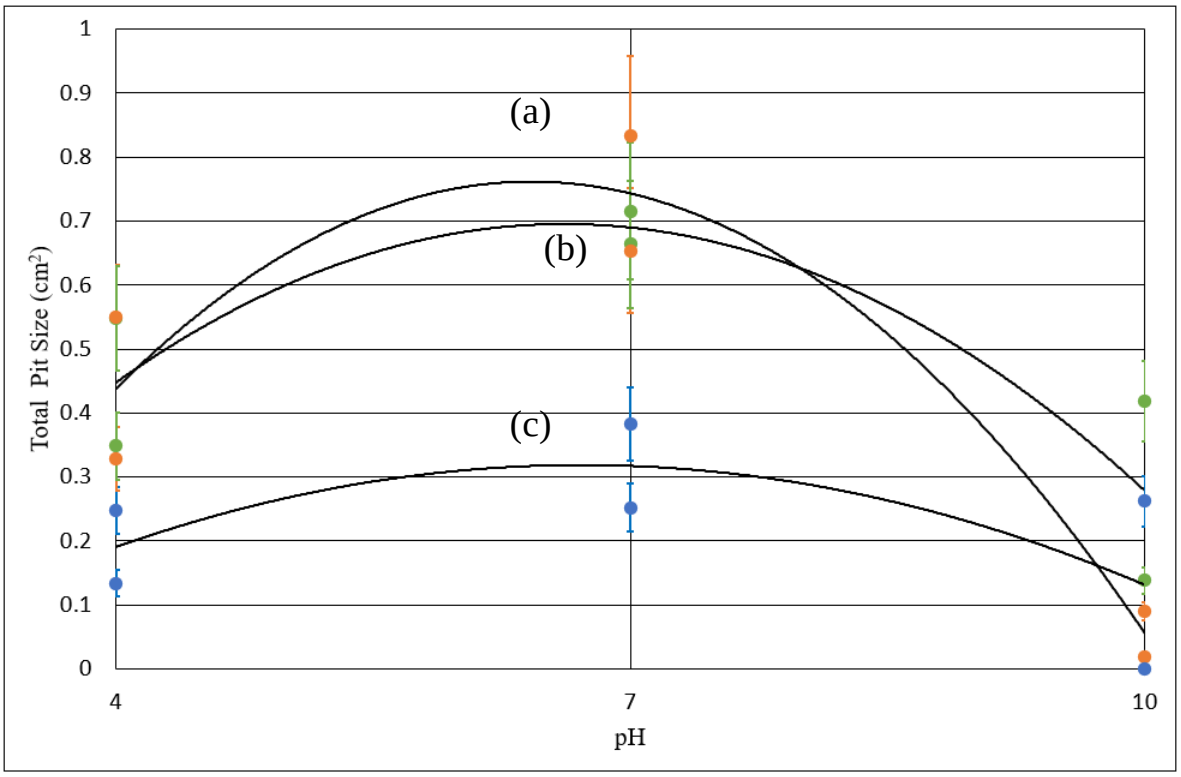

Figure 3.14: A graph showing total measured pit size for Ferralium (a), Zeron (b) and SAF (c) samples at 4, 6 and 10 pH.

3.3 Time-lapse Imagining (TLI) of CPT testing

The images gathered through the time lapse imagining can be seen in **Figures 3.15 – 3.17.** For each 3x4 grid of images the time increment increases by a constant value reading from left to right for each sample. Each material was tested twice with the TLI method to check for consistency, the sweep which provided the clearest set of images has been presented in this section. The current density response for the CPT of the sample materials was collected via a method identical to previous testing, **Figure 3.18**, to enable cross reference and consistency with the above CPT results. Some bubbles can be seen on the sample material in the figures, as to not have these confused with possible pits they have been highlighted as bubbles.

For the Ferralium sample in **Figure 3.15** image (a) the starting condition can be seen. As the test continues a group of small black dots, highlighted with arrows in images can be seen to from in images (b), (c), (d). These dots grow and begin to expel what looks to be a yellow brown cloud from the pit-like feature, as seen in images (e) to (k). Image (l) shows the state of the sample after the termination of the test. Comparing this to image (a) a clear difference can be observed; the sample has formed black dots or pit like features on the sample as well as a yellow brown deposit is present on the surface of the samples.

For the Zeron samples in **Figure 3.16** image (a) again shows the beginning of the test, prior to polarisation of the sample. Image (c) shows the formation of a pit-like feature in the top right of the sample. As the images / testing progresses this pit like feature does not appear to grow and develop beyond its original size and shape. Image (f) presents the formation of additional pit-like feature. As the test progresses from image (f) to image (k) a similar yellow brown cloud is pictured, appearing to originate from the pit-like features. The features also grow in apparent size as the test develops. Image (l) shows the sample after the polarisation of the material has been removed. It can be noted that the size of the pit-like features appear to be larger in diameter than that imaged in Ferralium sample, **Figure 3.15**.

For the SAF sample, as before, in **Figure 3.17** image (a) shows the beginning of the test, prior to polarisation of the sample material. As highlighted in image (d) a region of yellow brown cloud is beginning to form in the top right of the sample. As the test continues, from image (e) to image (k), the yellow brown clouded areas appear to form pit-like features. Again, the images are consistent with the cloud seemingly being expelled from the pit-like feature due to the feature being located at the centre of the cloud. Image (l) shows the sample material as the end of the CPT sweep. As with all the materials, when the polarisation is removed from the sample the yellow brown clouds cease to be emitted some the pit-like features. Further to this the features do not appear to

grow beyond this point. When comparing the relative size of the formed pit-like features it can be noted that those formed in the SAF material are smaller than that of the Ferralium and Zeron materials.

Figure 3.18 shows a plot of the current density against temperature from the TLI CPT testing for all three materials. It shows that the critical pitting temperature of the materials when undergoing the TLI investigation is consistent with the CPT data gathered for the respective materials in the above testing. The materials have followed a very similar current density change response to passing through the materials CPT, as presented by the shape of the graphs. The materials have also broken down at temperatures consistent with the above pH CPT testing. This means that there is little to no measured effect on the results of the testing caused by the adjustment to the test set up and methodology to the previous CPT testing, namely inverting the test specimen.

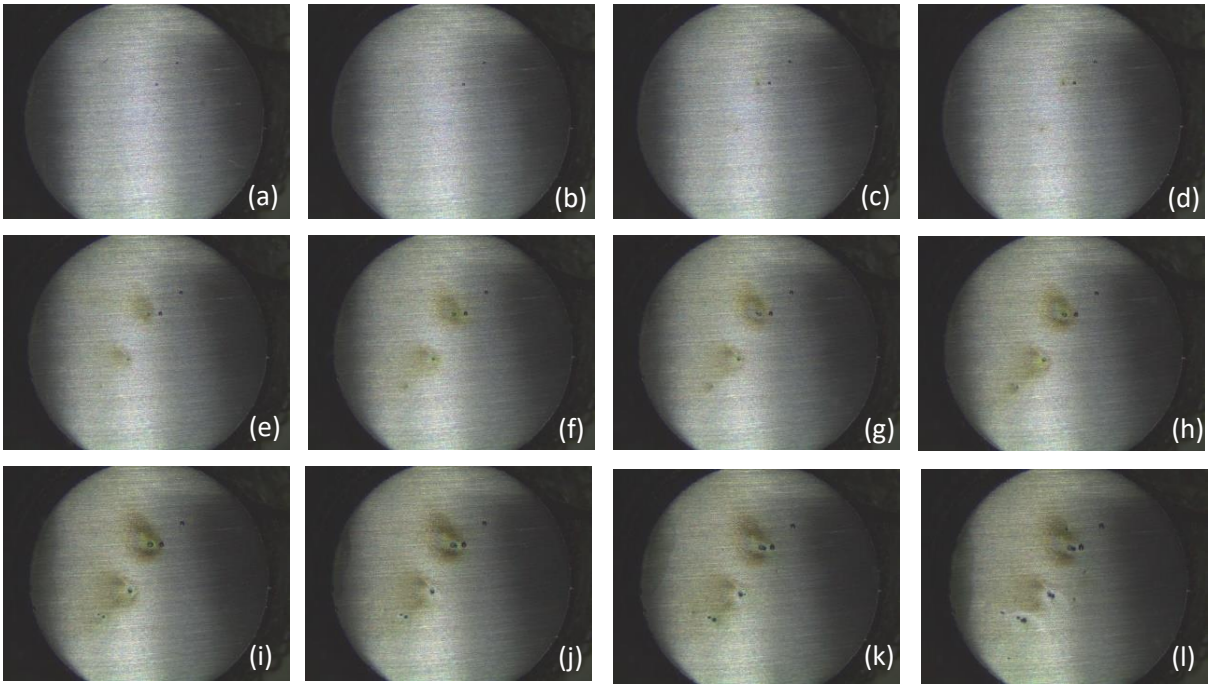

Figure 3.15: Time lapse images of CPT pit formation for Ferralium to show the formation and propagation of pits.

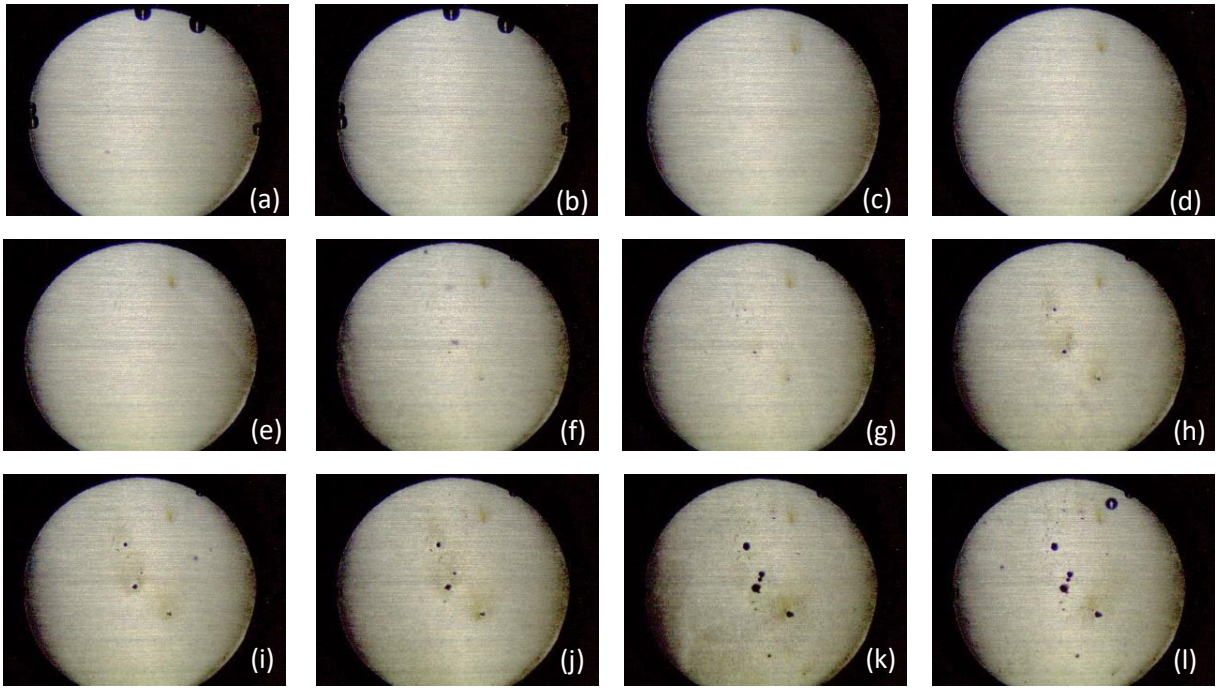

Figure 3.16: Time lapse images of CPT pit formation for Zeron to show the formation and propagation of pits.

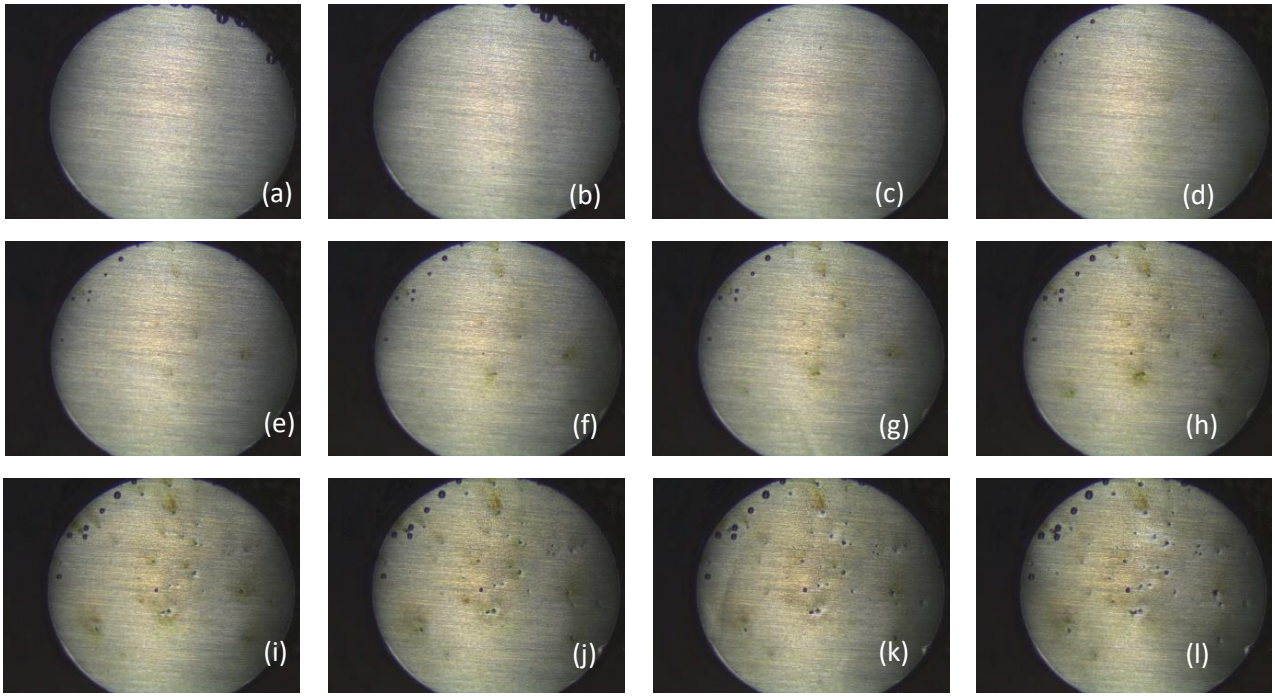

Figure 3.17: Time lapse images of CPT pit formation for SAF to show the formation and propagation of pits.

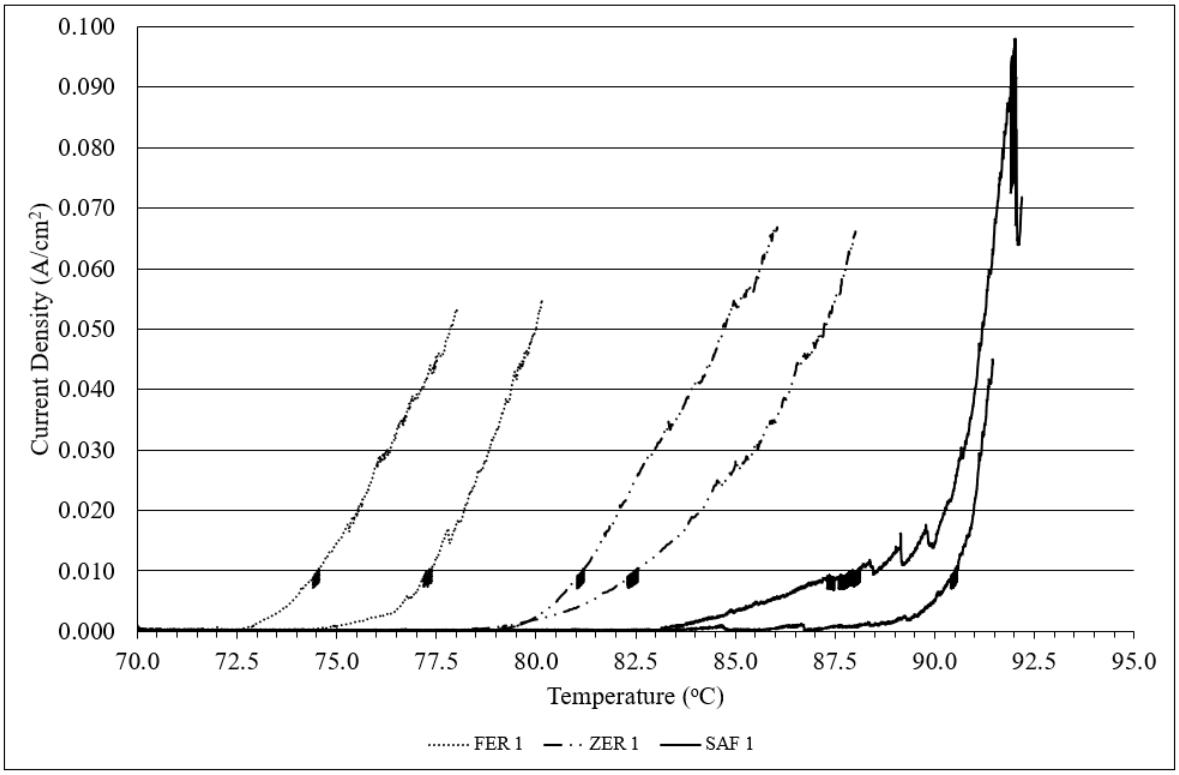

Figure 3.18: A graph showing the potentiostatic sweeps for Ferralium, Zeron and SAF samples at 7pH measured during TLI testing.

3.4 Pit Structure Image Analysis

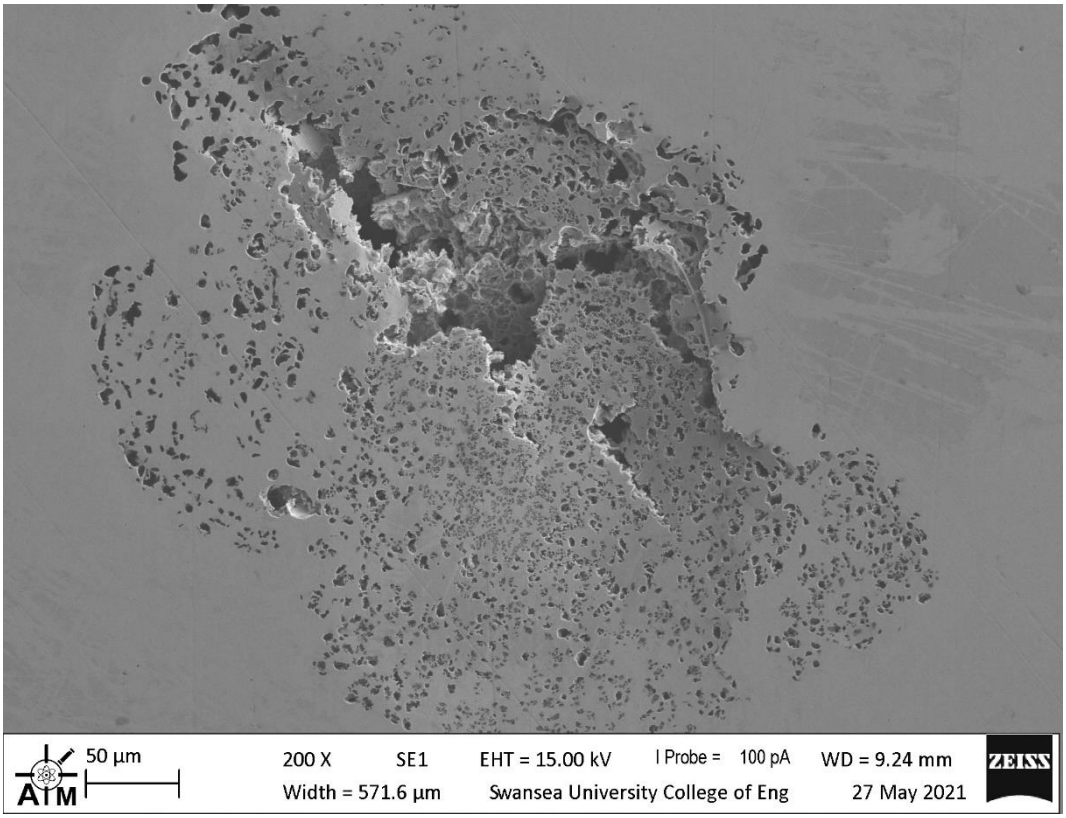

Figure 3.19: An SEM image of Ferralium with a lacy capped pit formed in 4pH 5% NaCl solution as it underwent a CPT sweep.

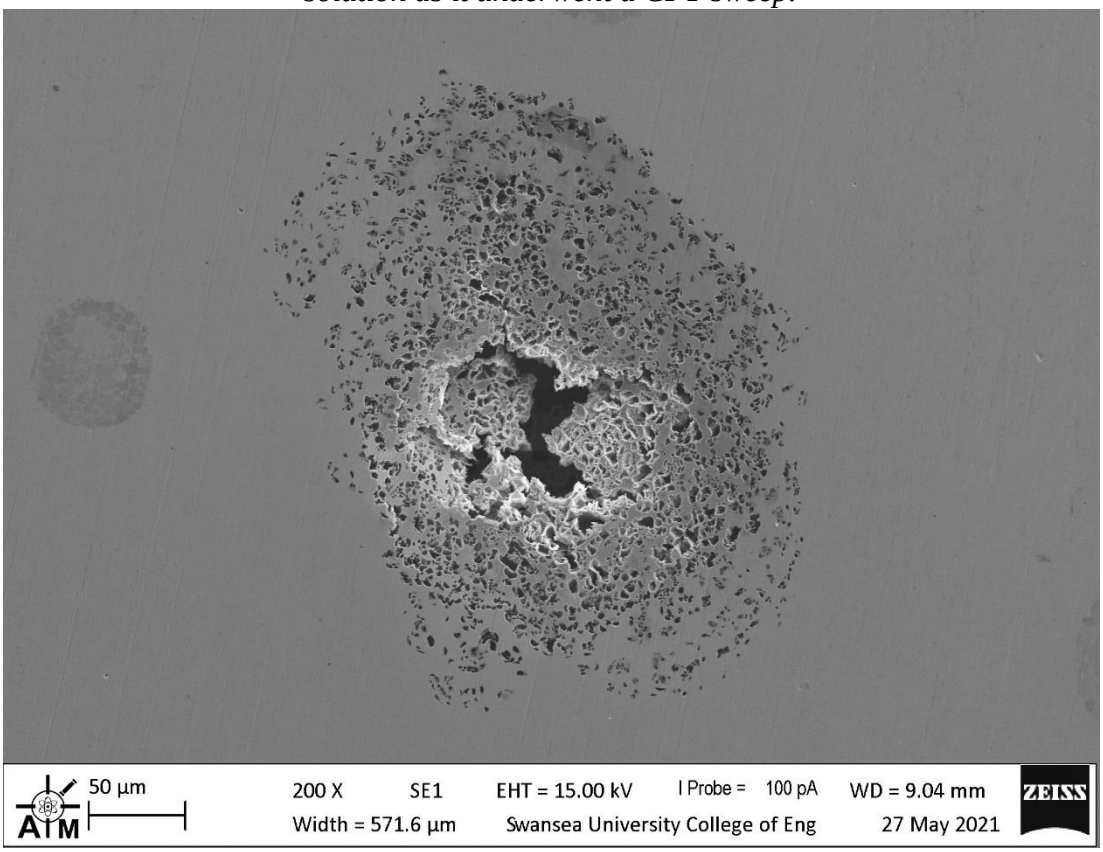

Figure 3.20: An SEM image of Ferralium with a lacy capped pit formed in 7pH 5% NaCl solution as it underwent a CPT sweep.

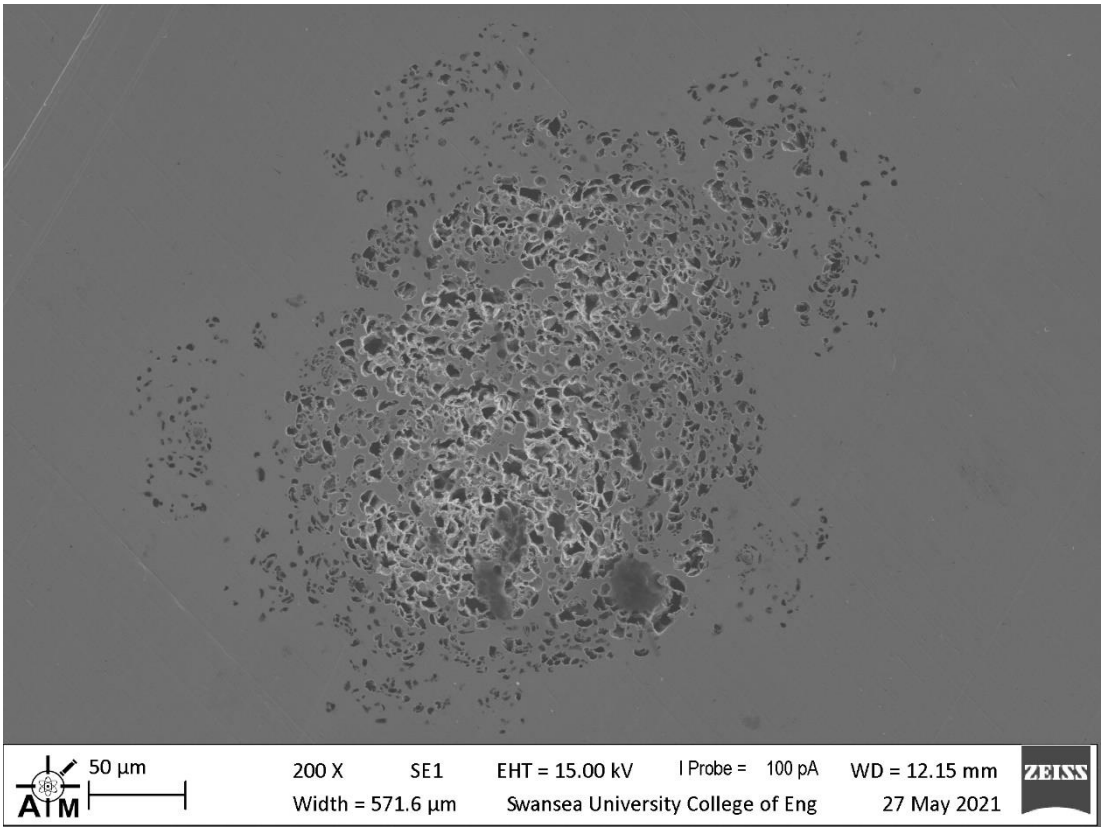

Figure 3.21: An SEM image of Ferralium with a lacy capped pit formed in 10pH 5% NaCl solution as it underwent a CPT sweep.

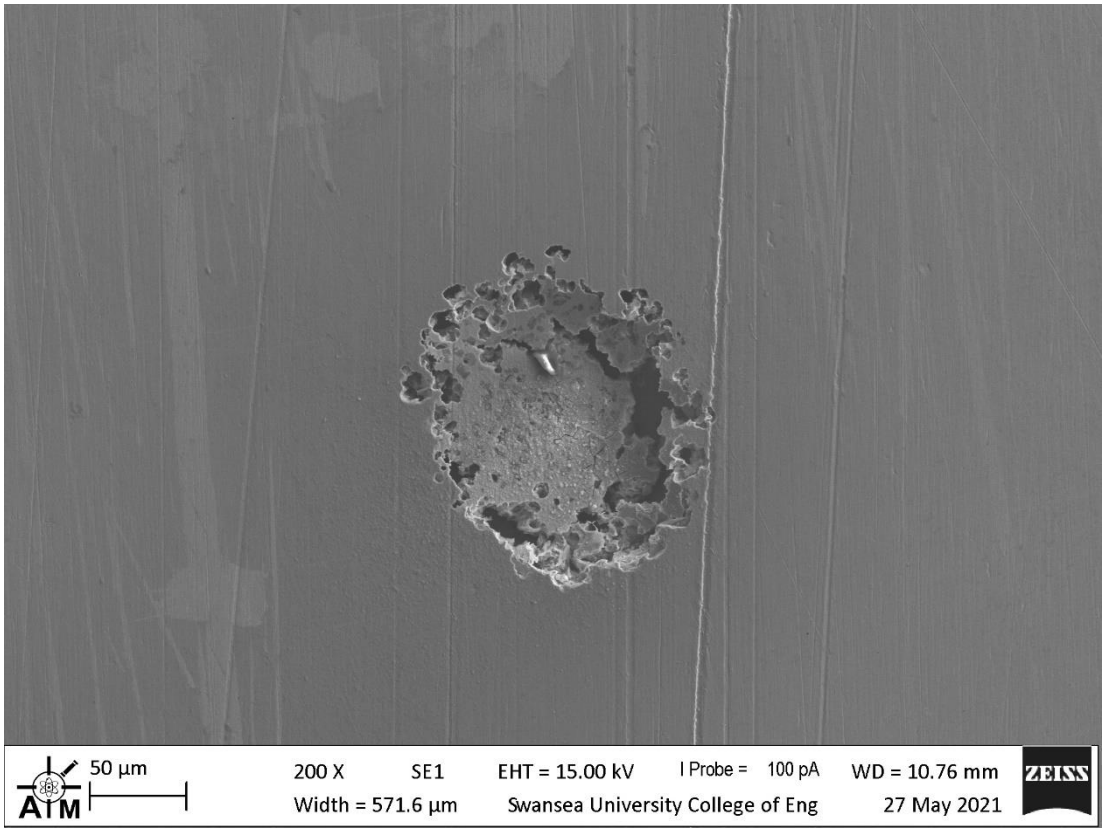

Figure 3.22: An SEM image of Zeron with a lacy capped pit formed in 4pH 5% NaCl solution as it underwent a CPT sweep.

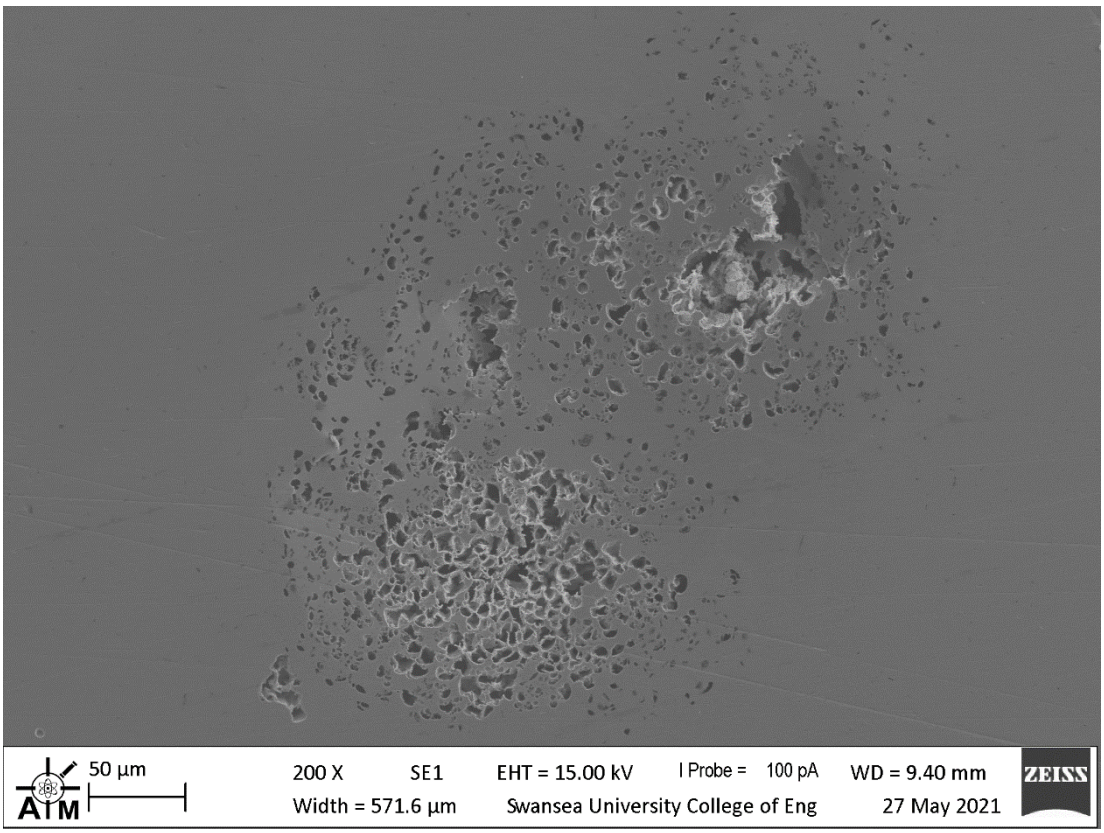

Figure 3.23: An SEM image of Zeron with a lacy capped pit formed in 7pH 5% NaCl solution as it underwent a CPT sweep.

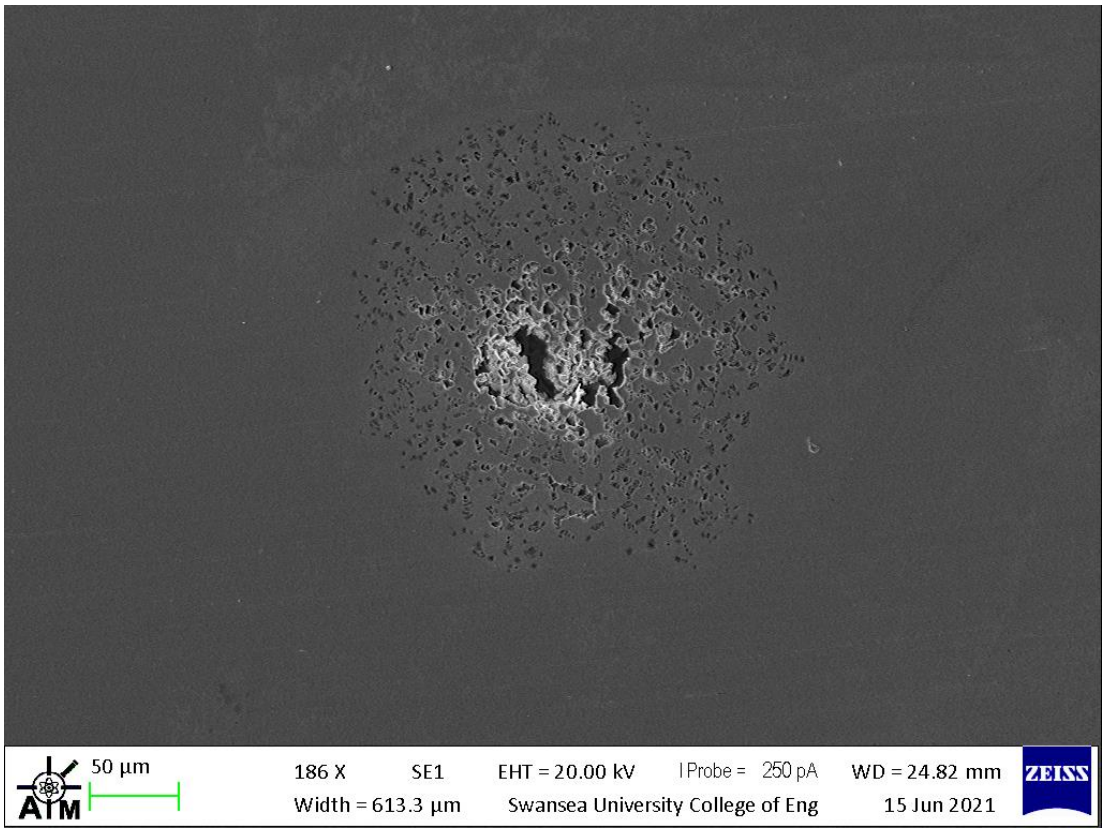

Figure 3.24: An SEM image of Zeron with a lacy capped pit formed in 10pH 5% NaCl solution as it underwent a CPT sweep.

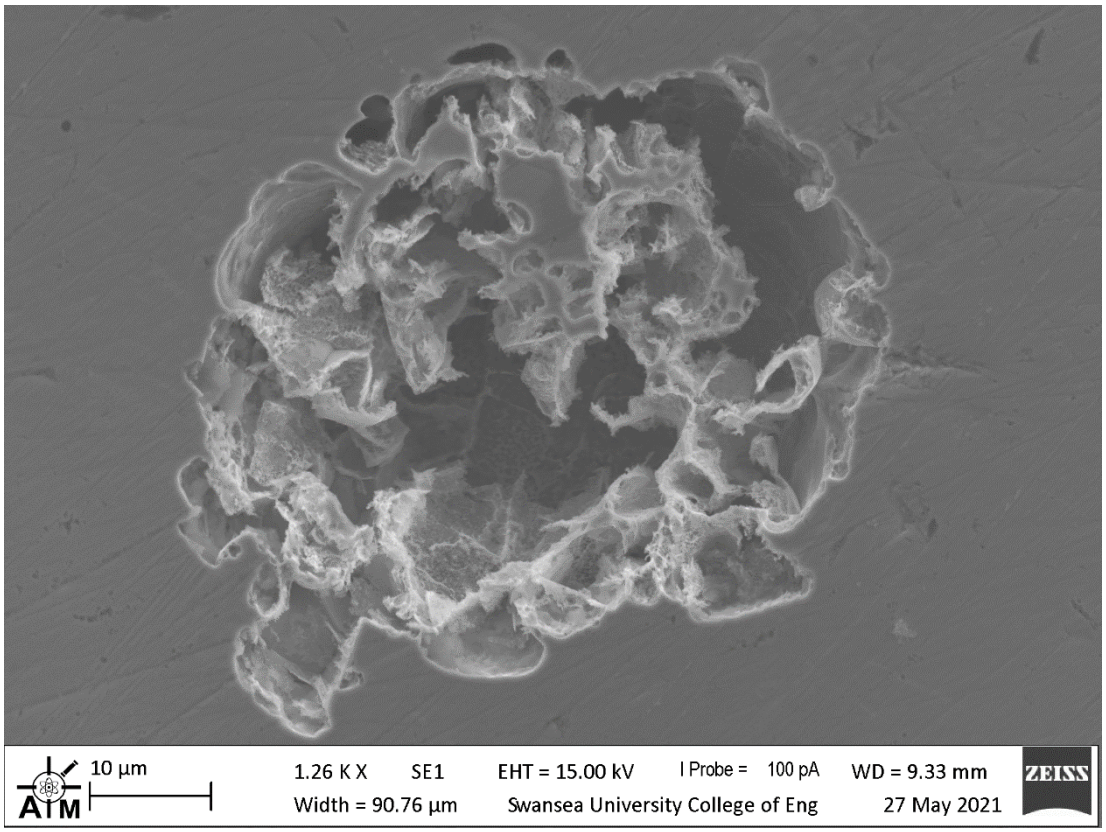

Figure 3.25: An SEM image of SAF with a lacy capped pit formed in 4pH 5% NaCl solution as it underwent a CPT sweep.

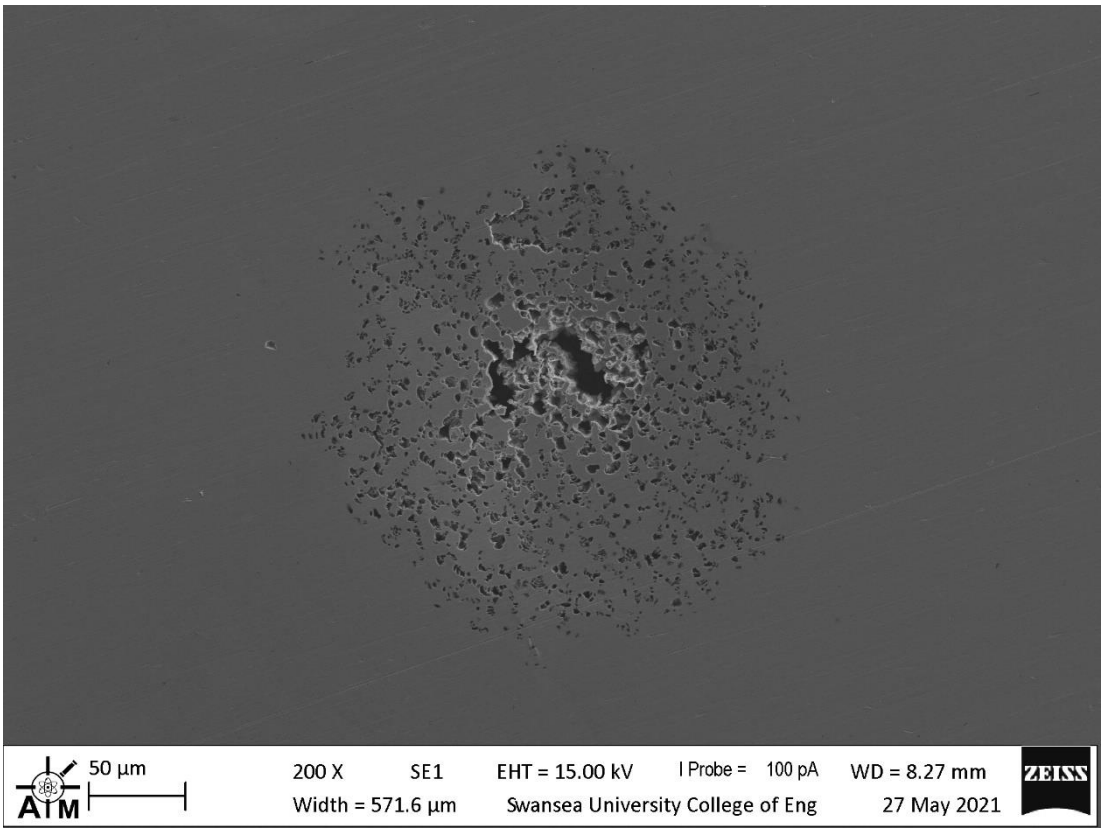

Figure 3.26: An SEM image of SAF with a lacy capped pit formed in 7pH 5% NaCl solution as it underwent a CPT sweep.

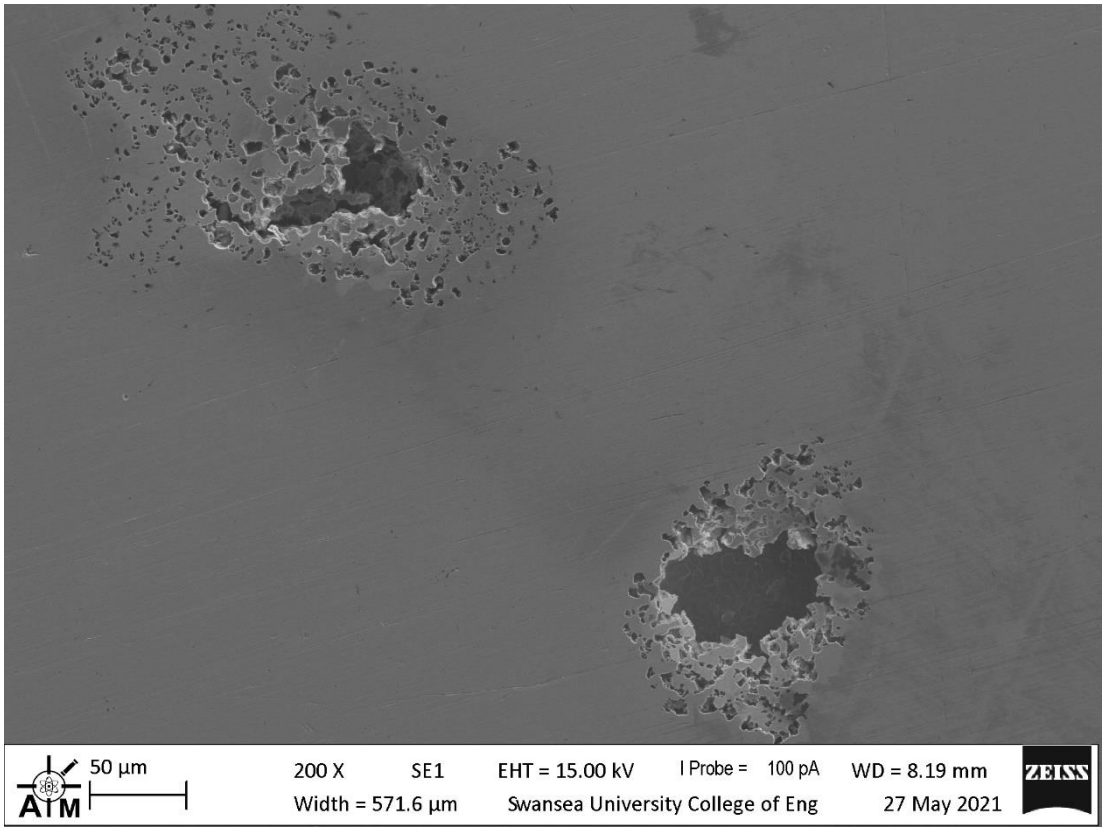

Figure 3.27: An SEM image of SAF with a lacy capped pit formed in 10pH 5% NaCl solution as it underwent a CPT sweep.

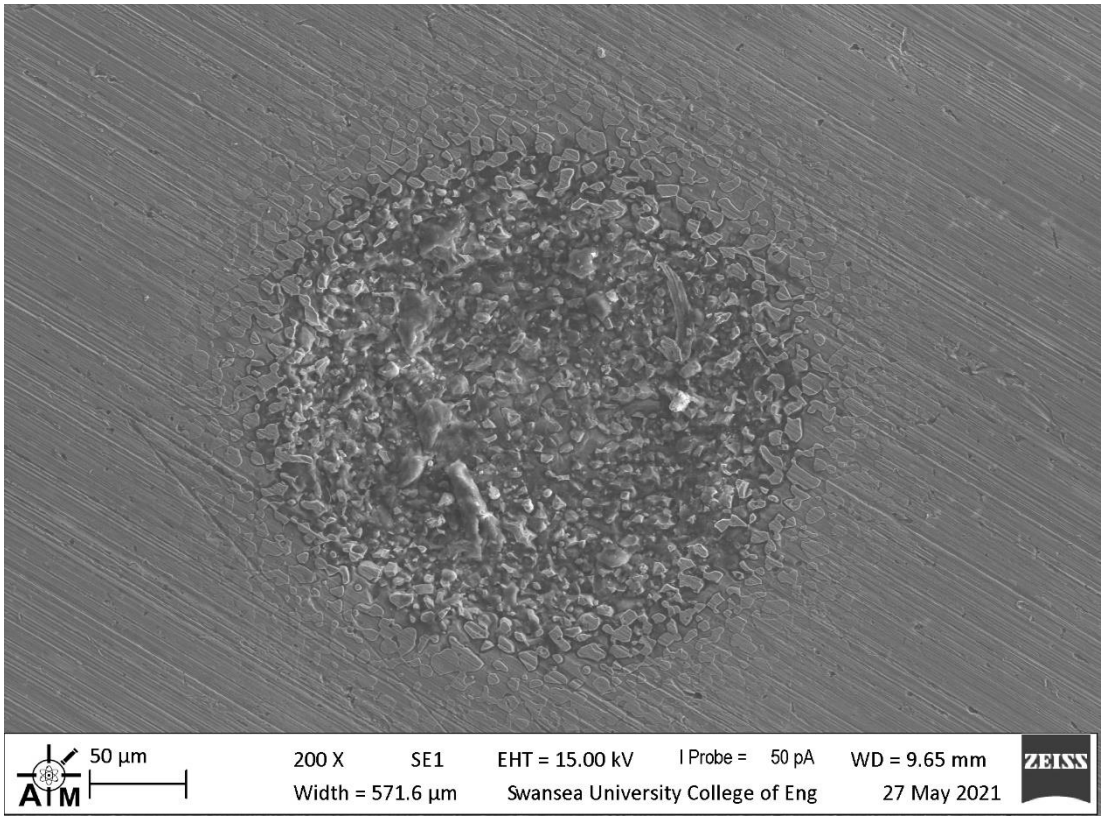

Figure 3.28: An SEM image of SAF with a pit formed from potentiodynamic polerisation in 7pH 5% NaCl solution..

Figures 3.19 – 3.27 show a representative image of the pits that formed on Ferralium, Zeron and SAF samples at 4pH, 7pH and 10pH respectively. In all of these images a lacy cap pit formation can clearly be seen.

Figure 3.28 shows a pit that formed through potentiodynamic polarisation with a SAF sample in 7pH solution. A difference can be seen when comparing against the lacy capped pits seen in Figures 3.19 – 3.27. Namely that there is no lacy cap present with this pit and there are features consistent with preferential phase corrosion. The lumpy, granular structure is likely from the ferritic structure of the SDSS preferentially corroding. This corrosion structure is consistent with previous investigations with potentiodynamic testing of SDSSs.

4.0 Discussion

4.1 Effect of break down time and surface roughness

The effect on surface roughness on the CPT of the materials is shown in **Figure 3.1**. The graph presented indicates that as the smoothness of the sample material increases so does the CPT, likely to be caused by increased energy required to initiate the pit formation. The reduced energy requirement could be caused by the rough surface having scratches in the surface locally increasing the concentration of corrosive solutions, in turn making the initiation of a pit more likely and requiring less energy. This is shown by the CPT decreasing with increasing surface roughness. SEM was used to assess if there was a difference in the structure of the formed pits, seen in **Figure 3.2**. No obvious difference in the structure of the pits can be seen, it is likely that the surface roughness only influences the initiation conditions of the pit and not the mechanism that drives its formation and growth. (48)

The length of time that the samples are polarised after they have transitioned through their CPT is directly linked to the formation and growth of pits. Therefore, it was key that the time after the material transitioned through its CPT was consistent to enable reliable comparison of pit size and numbers. A breakdown time of 6 minutes, shown in **Figure 3.3**, was selected to enable initiation, growth, and development of the pits. When the pits were looked at, with SEM, the 1 minute sample had no visible pits. The likely cause of this is due to the protective layer breaking down as the material transitions through the CPT, presenting as an increase in measured current density. However, as no pit was found, it is possible that the corrosion mechanism was not able to develop far enough to start the growth of a substantial pit. It is also possible that a pit had formed and was not located during the SEM investigation.

A singular pit was found, formed on the 3 minute sample after the CPT breakdown time test. The formed pit appeared to be consistent with pits that

were imaged later in the CPT investigation. However, it was deemed that the small sample size of the formed pits would not be enough to gain suitably reliable data on the structure of the pit

The sample that was allowed to develop 6 minutes after the increase in measured current density produced many pits. It was deemed that 6 minutes after the CPT breakdown would be used for the further testing to enable suitable initiation, growth, and development of the pits.

The measured current density is proportional to the amount of corrosion that is occurring at a given moment. When the current density is higher there are more ions flowing through the material, meaning more area of the material is undergoing active corrosion. As the peak grows in value a larger area of the material is being broken down. Meaning that as the material moves further above the temperature at which it starts to breakdown more and more corrosion is occurring in the material. This could be caused by the growth in total size of pits or the initiation and formation of more pits. (47) (49) (26)

4.2 Effect of pH on Critical Pitting Temperature

As presented in **Figures 3.11** and **3.12,** the measured CPT and the 0.001 A/cm^2 CPT for each material there is very little change in the critical pitting temperature. The effect is even less when looking at **Figure 3.12** with the offset reducing the potential error with measuring the CPT. The effect of pH in the solutions used had very little change over the breakdown temperatures of the materials.

When comparing the materials against each other a clear difference is noted. There is a clear and measurable grouping of the results for each material. It is clear that Ferralium has displayed the lowest measured CPT temperature, with approximately 76^{o}C across the three tested pH solutions. Zeron has the next highest measured CPT of approximately 85^{o}C, with SAF having the highest measured CPT of approximately 89^{o}C.

Assessing the data presented in **Figure 3.4** there is high repeatability of the measured breakdown temperatures. It can also be noted that there is a correlation of the profile produced after CPT for each material. The individual behaviour post breakdown of each material is unique. With Zeron samples producing a low current density reaction post break down, shown by the graphs of each response remaining below 0.003 A/cm^2. The Ferralium samples also have correlation of the current density response profiles, with a higher current density response to that of the Zeron samples. SAF samples displayed the highest measured current density response post CPT breakdown. Further to this observation it can be noted that the average gradient of the current density responses to temperature change is different depending on the material. With Zeron samples having the lowest gradient and SAF samples having the highest gradient.

Acidification and alkalisation of the solutions had little to no measurable effect on the CPT of the materials under test. It is therefore unlikely that the pH of the NaCl solution that the SDSS are exposed to influences the CPT behaviour and repose of the material indicating that the mechanism which drives the formation of the pits, in a CPT response, is not reliant on the bulk pH in the surrounding solution (50). This could be due to the local conditions in and around the pits, during their initiation and as they grow, has a dominating effect vs the surrounding bulk electrolyte. With areas around the pits having local concentration of acidic electrolyte even if the bulk is alkaline.

4.3 Effect of Copper and Tungsten Addition on Critical Pitting Temperature

The difference in the measured CPT of the materials can be deemed as being driven by the composition of each material, as this is the only variable present in the test. Ferralium has the highest level of copper present in the

microstructure, 1.5 - 2.0 wt%. The percentage of copper decreases from Ferralium to Zeron, with 0.5 - 1.0 wt%. SAF has the lowest level of copper with <0.5 wt%. It is likely that the copper is causing a detrimental effect on the measured critical pitting temperature behaviour of each material. It is possible that the copper is increasing the thermodynamic likelihood of pit initiation when transitioning through CPT. The detrimental effect could be caused by an electrochemical reaction being more favourable with the presence of copper in the microstructure of the material. However, it is likely this would present itself as a difference in measured OCP. Prior to each CPT run the OCP of the material was measured and recorded, the results of which can be seen below in **Figure 4.1**. There is little measured difference between the OCPs of the three materials with their values varying between -0.045 – -0.064 Volts of the applied polarisation and their scatter presenting a negligible relative difference in average OCP at 70°C when compared to polarisation of 0.9 Volts The range in values is less than 3% compared to the polarisation voltage. Further to this, no clear trend is shown on the effect of pH on the materials OCP at this temperature.

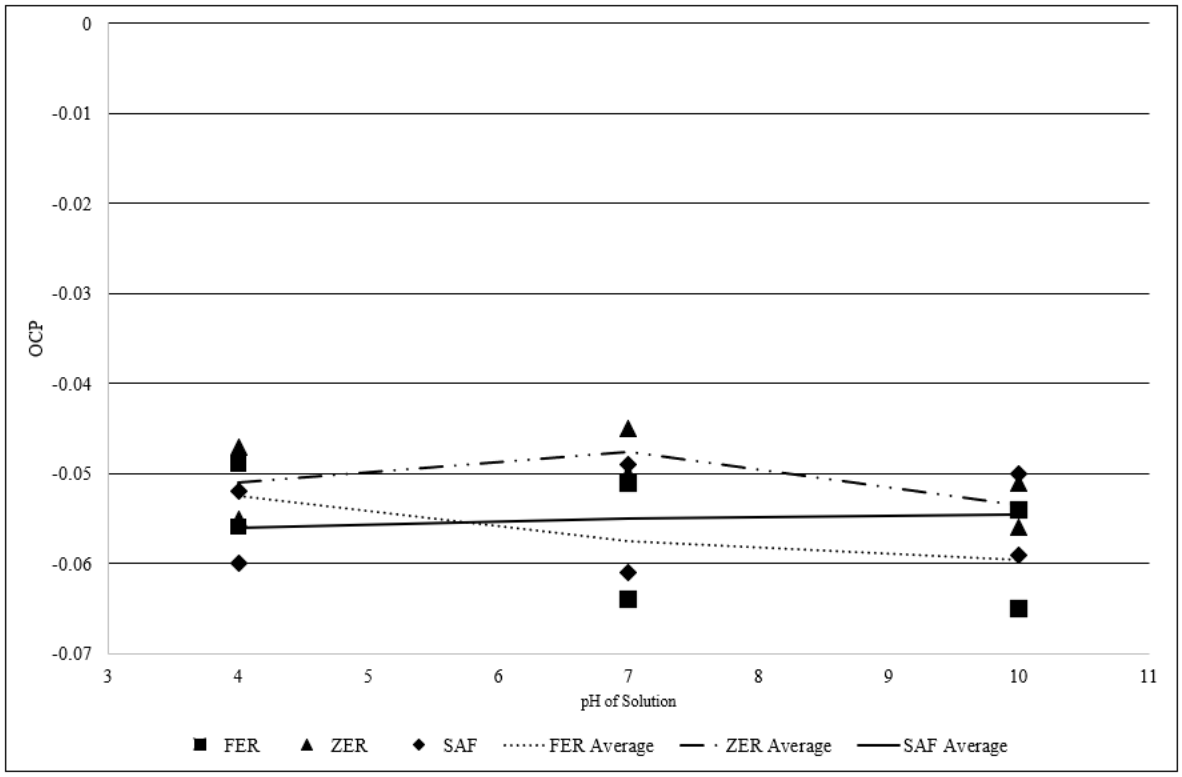

Figure 4.1: A graph showing the measured OCP voltages prior to CPT testing at 70° for Ferallium, Zeron and SAF in 5% NaCl solution with vaying pH.

Zeron has a level of tungsten in its composition, it is unclear if this element is having an effect on the measured CPT of the material as the level of copper in all of three materials under test decreases. It is possible that the tungsten is influencing the behaviour of the material during the testing however. It is possible that tungsten is affecting the response of the material after breakdown, as noted by the smaller peaks displayed in the Zeron samples, indicating that Zeron samples were relatively more electrochemically 'stable' than the other materials after the CPT breakdown. Ferralium and SAF, both lacking W in their composition, have a similar current density response after breakdown further supporting the possibility W is affecting the breakdown response of Zeron. (51)

4.4 Mechanism of critical pitting temperature pit formation

As **Section 3.4** shows all pits formed whilst under CPT, independent of material, formed a lacy capped pit structure. The pit structure and driving mechanism is different to the pits formed through Potentiodynamic polarisation testing. The lacy capped pit structure is consistent throughout all the materials, all surfaces roughness, all breakdown times, and all pHs that the SDSSs were tested for CPT behaviours. It is certain that when the SDSS materials are undergoing breakdown in a CPT situation they pit through the lacy cap mechanism. In the potentiodynamic polarisation pit formation mechanism there is evidence that the corrosion is preferentially attacking one of the phases of the SDSS. In the CPT breakdown behaviour, there is evidence to show that there is little preferential attack on the individual phases of the SDSS. In **Figure 3.28** a facetted structure and shape is present in the potentiodynamic pit, which is very regular and circular in overall shape, grain boundaries are visible in the surface of the pitted structure which presents an etched-like appearance.

Note **Figure 3.5**, one of the responses of the Zeron material has as saw tooth patten, with a peak in current density beginning to form which then returns to zero and then peaks again. It is likely that this is caused by the formation of singular pit, which is initiated and starts to grow. But then for some reason the pit stops developing and results in a pause in the corrosion behaviour of the material. The current density then peaks again, likely to the initiation of a new pit. The peak again suddenly drops in current density, indicating that the pit has stopped corroding. It is highly likely that this is caused by the cap of the lacy cap pit structure, through some means, falling away from coving the pit. In turn, removing the pit as an electrochemically favourable system.

It can be concluded that the mechanism that drives the corrosion behaviour of the SDSSs relies on the presence of a cap to allow the local composition of the solution to be favourable to corrosion. When the caps of the pits are lost the composition of the internals of the pit become closer to the bulk material and

means that the mechanism of corrosion is no longer possible in that location, requiring the material to re-initiate a pit with a cap present. It is likely that when a sudden drop in current density is measured in the corrosion response of a material, it is caused by a cap of pit failing causing the pit to 'die'. An example of a pit that has lost its lacy covering can be seen in **Figure 3.26**. In this image the evidence of a lacy structure can be seen on the edges of the pit, but the cover which protects the internal environment of the pit has been lost. It is unlikely that this was lost between the test and the SEM imaging as only a very light cleaning was conducted with an Ethanol rinse. Little to no mechanical cleaning was used that could have removed the pit. Therefore, it can be concluded that the pit lost its cap during the test. This is further support by the overall size of the pit being smaller than more developed pit. It is likely that as this pit started to develop it lost the cap which then caused it to die prematurely which resulted in its reduced size.

Across all three of the materials such a sharp and sudden drop can been seen in the corrosion response. When the current density does not return to 0 $A.cm^2$ this is possibly due to multiple pits present in the material corroding and one or more of the pits passivating. The corrosion of the material does not completely stop as there are still pits present in the material that have not passivated and continue to corrode.

4.5 The Effect of pH on Pit Size

Figure 3.13 showing the average pit size present in each of the materials against the pH at which there were tested presents some clear differences. For all the SDSS the measured average pit size is higher when they were tested in 7 pH than when under test in the 10 pH and 4 pH. Overall, at each pH Ferralium formed the largest pits and SAF formed the smallest on average. It is unclear as to the reason why Ferralium formed larger pits than the other materials. However, it is possible that this is also linked to the elevated levels of copper in Ferralium composition. It is possible that the mechanism that causes Ferralium

to transition through its CPT at a lower temperature also influences the growth mechanism of the pit.

Conversely it is possible that the SAF material performed better when it comes to average pit size due to its reduced level of copper. It does not appear to be likely the elevated levels of tungsten in the Zeron material has affected the average pit size formed during CPT breakdown.

There is a similar trend to above seen in **Figure 3.14** with the total pitted area. There is a notable variation with the Ferralium material forming a smaller total pitted area at 10pH against the other materials. It is possible that the copper present in the material is benefiting the materials response in this condition when it comes to total area, driving the material to produce more smaller pits against the other materials. There was, however, no clear reason as to why the total pitted area is lower for Ferralium at 10pH. At 7pH and 4pH however the trend is consistent with that of the previously mentioned average pit size and is likely to be associated with the same causal mechanism of increased copper concentration.

4.6 Timelapse imaging of CPT

The imaging of the materials whilst they transitioned through their CPT was conducted to enable confirmation that pits were initiating as the materials began to have a current density response. Further to this TLI was able to provide insights into the mechanism driving the initiation and growth of the pits. The TLI set up was successful in capturing the formation and growth of lacy capped pits in a NaCl environment for all of the SDSSs alloys. The pits that formed from the TLI CPT test were investigated with SEM and showed that all pits had formed lacy capped pits, consistent with that of the pH testing.

In the TLI a correlation of the initiation of the pits and beginning of the current density response can be observed. As the current density begins its peak, pits can be seen forming on the surface of the material.

It is significant that a yellowish brown cloud is seen around the active pits, it is possible that this is caused by the evolution of chlorine from the pit or corrosion product. The yellowish brown cloud ceased to be evolved from the material when polarisation was stopped and was not present on the surface of the material when removed from the solution. It therefore indicates that there is a very high concentration of chloride around and in the pits. It is possible that if the pit loses its cap, then the concentration of chloride ions decreases to the extent that the pit dies. This can be seen in **Figure 3.16** were there is a pit formed which then appears to cease growing and evolving a cloud. In this example it is highly likely that a cap is lost, and the subsequent passivation of the pit can be seen.

The chloride ion concentration is important to the development of the pit as it is widely agreed that the chloride ions interact with the passive oxide layer causing it to be destabilised (13) (14) (28).

5.0 Conclusions

The Critical Pitting Temperatures of Ferralium, Zeron and SAF were investigated to look at the effect of pH on the measured CPT and to understand the type of mechanism driving the formation and growth of the pits. The effect of copper and tungsten addition on the measured CPT could also be investigated. Due to the elevated copper concentration in Ferralium alloy, compared to the other alloys, and the elevated tungsten concentration in the SAF, alloy compared to the alloys.

Initial assessment was carried out on the effect of surface roughness of a Ferralium sample on the CPT. It was found that the higher the surface roughness of the samples the lower its measured critical pitting temperature. This is deemed to be likely due to the increased surface roughness of the material enabling easier initiation of the pits, possibly due to preferential micro-climates resulting in a lower measured CPT.

Assessment was conducted on the optimum time to allow the corrosion reaction to progress after the CPT had been surpassed. This was tested on a Ferralium sample, and it was found that allowing the sweep to continue for 6 minutes after a measured CPT produced a notable number of pits that had been well developed.

The results for the surface roughness and breakdown time investigations fed into the development of a robust methodology for assessing the critical pitting temperature of the SDSS alloys for the further testing.

An investigation into the effect of the pH, of the test solution, on the three alloys was conducted. All three alloys underwent a CPT test sweep at 4pH, 7pH and 10pH.

Little to no effect on the individual alloys CPT was measured as a result of changing the solutions pH. For all the alloys their CPT was consistent regardless of the pH of the solution.

A clear difference was measured in the CPT of the individual alloys, they all had a measurable and notable difference in measured critical pitting temperature. This consisted of the copper rich alloy (Ferralium) having an average CPT of 76^{o}C across the three tested pH solutions. The low copper alloy (Zeron) having the next highest measured CPT of 85^{o}C. With the tungsten rich alloy (SAF) having the highest measured CPT of 89^{o}C.

This result differs from previous potentiodynamic polarisation studies where little to no measurable differences between the individual alloys was found. (46)

The reasons for the different measured CPT of the individual alloys is unknown. However, it is likely to do with the respective copper and tungsten additions. It is possible the mechanism through which the copper addition is affecting the measured CPT is down to it redepositing as pure copper and causing galvanic corrosion or that it destabilises the passive layer of the material. This could be investigated by conducting EDS measurements on the regions around the formed pits, gathering copper concentration information, and comparing the three materials. If there is a measured increase of copper concentration around or in the pits it therefore likely to be a mechanism that is occurring.

It is unclear whether the higher measured CPT of the SAF alloy is due to it having an elevated level of tungsten or because it has lower levels of copper in its alloy. There is a trend between the three alloys that as the copper concentration decreases the measured CPT of the alloys increase.

There is a measured effect of the pH on the average pit size that the alloys formed. For all three alloys they formed larger pits when undergoing CPT sweeps in 7pH solution compared to 4pH and 10pH solutions. The mechanism that has caused this is unknown. There is also a difference in the pit size of the individual alloys This consisted of the copper rich alloy (Ferralium) having the largest measured pits on average. The low copper alloy (Zeron) having the next largest measured pits. With the tungsten rich alloy (SAF) having the smallest

measured pits. The reason for this difference is unclear however it is again possibly due to the copper concentration in the induvial alloys having a detrimental effect on the passive layers' behaviour in CPT corrosion environment.

SEM imaging of the pits that formed found that the pits that had formed in all of the CPT sweeps for all of the alloys had formed a pit structure known as lacy capped pits. This cap on the pit is likely to enable concentrations of the solution on the internal of the pit to be high enough to encourage corrosion of the highly corrosion resistance super duplex stainless steels. There is no visible difference in the structure of the lacy capped pit formed in the individual alloys. It is likely that copper and tungsten additions have little to no effect on the mechanism that causes the initiation and growth of the lacy capped pit as lacy capped pits can form in materials that do not have copper or tungsten present in their structures (27)

Time-lapse imagery of the samples undergoing CPT sweeps was conducted to confirm that the pits were forming after the alloy transitioned through its critical temperature. The measured CPT of the individual alloys were consistent with those measured in the previous 3 investigations. The TLI was able to capture the formations of the pits as the material transitioned through its critical temperature. It is possible that re-passivation of the pits were captured in the TLI. The re-passivation is likely to be caused by the lacy caps of the pits being removed or degrading. The loss of the cap results in the internal environment of the pit to no-longer be conducive to continuation of the corrosion reaction.

5.1 Further work

To expand on the results presented in the study it is recommended that further work is conducted into understanding the mechanism that is driving the formation of the lacy capped pits in the SDSSs during a critical pitting

temperature sweep. It is recommended that work is done into understanding how copper is affecting the formation and growth of the pits during a CPT sweep.

6.0 References

[1] **Newman, John and Balsara, Nitash P.** *Electrochemical Systems.* s.l. : Wiley, 2021.

[2] *Electrochemical Cells.* **Ikenna Chibuzor Emeji, Onoyivwe Monday Ama, Uyiosa Osagie Aigbe, Khotso Khoele, Peter Ogbemudia Osifo & Suprakas Sinha Ray.** 65-84, s.l. : Springer, 202, Vols. Nanostructured Metal-Oxide Electrode Materials for Water Purification.

[3] *Computation of free energy.* **WF Van Gunsteren, X Daura, AE Mark.** s.l. : Helvetica Chimica Acta, 2002. 3113-29..

[4] *Thermodynamics of solvation of ions. Part 5.—Gibbs free energy of hydration at 298.15 K. .* **Y., Marcus.** 87(18):2995-9., s.l. : Journal of the Chemical Society, Faraday Transactions. , 1991.

[5] *Electrochemical series. CRC handbook of chemistry and physics.* **P., Vanysek.** 8:8-33., 2000.

[6] *Electrochemical parametrization of metal complex redox potentials, using the ruthenium (III)/ruthenium (II) couple to generate a ligand electrochemical series. Inorganic Chemistry. .* **AB., Lever.** 1990 Mar;29(6):. 1271-85..

[7] *Passive films on stainless steels—chemistry, structure and growth. Electrochimica acta. .* **Olsson CO, Landolt D.** 20;48(9):1093-104., 2003 Apr .

[8] *Effect of high anodic polarization on the passive layer properties of Superduplex stainless steel friction stir welds at different chloride electrolyte pH values and temperatures.* **Santa-Cruz, L., Machado, G., Vicente, A., Hermenegildo, T. and Santos, T.** s.l. : nternational Journal of Minerals, Metallurgy and Materials, 2019.

[9] *The passive state of stainless steels. Materials Science and Engineering. .* **I., Olefjord.** 1980 Jan . 1;42:161-71..

[10] *Mechanism of crevice corrosion. Corrosion. .* **Rosenfeld IL, Marshakov IK.** 1964 Apr 1. ;20(4):115t-25t..

[11] *Crevice corrosion of stainless steels: I. A mathematical model. British corrosion journal. .* **Oldfield JW, Sutton WH.** 1978 Jan 1;. 13(1):13-22..

[12] *Pitting and crevice corrosion. .* **Szklarska-Smialowska, Z. and ZS-Smialowska,.** s.l. : NACE nternational. , (2005).

[13] **GS., Frankel.** *Pitting corrosion. ASM handbook.* 2003. ;13:236-41..

[14] *Pitting Corrosion of Metals. .* **Frankel, G.** s.l. : Journal of The Electrochemical Society, , (1998). .

[15] *Revised pourbaix diagrams for iron at 25–300 C. Corrosion Science.* **Beverskog B, Puigdomenech I.** 1996 Dec 1;. 38(12):2121-35..

[16] *The absolute potential of the standard hydrogen electrode: a new estimate. The Journal of Physical Chemistry. .* **Reiss H, Heller A.** 1985 Sep;. 89(20):4207-13..

[17] *Thermodynamics of Corrosion: Pourbaix Diagrams. Introduction to corrosion science. .* **McCafferty, E.,.** s.l. : Springer, (2010). .

[18] **Ives DJ, Janz GJ.** *Reference electrodes. Academic Press, New York; .* 1961.

[19] *Critical pitting temperature measurements of stainless steels with an improved electrochemical method. Corrosion Science. .* **R., Ovarfort.** 29(8):987-93., 1989 Jan 1;.

[20] *Temperature dependence of pitting potentials for austenitic stainless steels above their critical pitting temperature. .* **Laycock NJ, Newman RC.** s.l. : Corrosion science. , 1998 Jun 1;, Vols. 40(6):887-902.

[21] *ASM handbook.* **Moosbrugger C, Sanders BR, Anton GJ, Hrivnak N, Kinson J, Polakowski C, Muldoon K, Henry SD, Scott Jr WW. Cramer SD, Covino Jr BS, editors.** Ohio: : ASM international; , 2003., Vols. Materials Park, .

[22] *Effect of pitting nucleation on critical pitting temperature of 316L stainless steel by nitric acid passivation. .* **Liu J, Zhang T, Meng G, Shao Y, Wang F.** s.l. : Corrosion Science. , 2015 Feb 1. ;91:232-44..

[23] *Corrosion Behavior of Duplex Stainless Steels in Acidic- Chloride Solutions Studied with Micrometer Resolution.* **Femenia, M.** (2003). .

[24] *In situ study of selective dissolution of duplex stainless steel 2205 by electrochemical scanning tunnelling microscopy. .* **Femenia, M., Pan, J., Leygraf, C. and Luukkonen, P.** s.l. : Corrosion Science, (2001). .

[25] *Critical pitting temperature for Type 254 SMO stainless steel in chloride solutions. .* **Abd El Meguid, E. and Abd El Latif, A.** s.l. : Corrosion Science, (2007). .

[26] *In situ monitoring of the microstructural corrosion mechanisms of zinc–magnesium–aluminium alloys using time lapse microscopy.* **Sullivan, J., Mehraban, S. and Elvins, J.** s.l. : Corrosion Science, (2011).

[27] *Evolution of current transients and morphology of metastable and stable pitting on stainless steel near the critical pitting temperature.* **Moayed MH, Newman RC.** 48(4):1004-18., s.l. : Corrosion science. , 2006 Apr 1;.

[28] *Effect of temperature, chloride concentration and sulphate addition. .* **Ernst P, Newman RC. Pit growth studies in stainless steel foils. II.** 44(5):943-54., s.l. : Corrosion science. , 2002 May 1;.

[29] *Super duplex stainless steels.* **Nilsson, J.** 1992, Materials Science and Technology,, pp. 685-700.

[30] *The effect of copper addition on the corrosion resistance of cast duplex stainless steel. .* **de Lima HM, Tavares SS, Martins M, Araújo WS.** 8(2):2107-19., s.l. : Journal of Materials Research and Technology. , 2019 Apr 1;.

[31] *Effects of Mo, Cu, Si and P on Anodic Behavior of 17 Cr Steels, .* **LIZLOVS, E. A.** s.l. : CORROSION. , (1966). .

[32] *Characterization of microstructure, chemical composition, corrosion resistance and toughness of a multipass weld joint of superduplex stainless steel UNS S32750. .* **Tavares SS, Pardal JM, Lima LD, Bastos IN, Nascimento AM, De Souza JA.** s.l. : Materials Characterization, 2007 Jul 1;58(7): 610-6.

[33] *Effect of Copper on Active Dissolution and Pitting Corrosion of 25% Cr Duplex Stainless Steels. .* **Garfias-Mesias, L. and Sykes, J.** s.l. : CORROSION, , (1998). .

[34] *Effect of tungsten on the pitting and crevice corrosion resistance of type 25Cr super duplex stainless steels. .* **Haugan EB, Næss M, Rodriguez CT, Johnsen R, Iannuzzi M.** 73(1):53-67., s.l. : Corrosion. , 2017 Jan 1;.

[35] *Pitting Corrosion of Super Duplex Stainless Steel-Effect of Tungsten and Isothermal Heat Treatments. .* **Østvold, H.K.** (2017). .

[36] *Effect of tungsten on the precipitation kinetics and localized corrosion resistance of super duplex stainless steels. .* **Bernås, M., Westermann, I., Jernberg, A., Qvale, A.H., Johnsen, R., Torres, C. and Iannuzzi, M.** s.l. : NACE-International , (2018). .

[37] *Influence of Tungsten on Passivity Breakdown and Repassivation of 25CR Super Duplex Stainless Steel. .* **Torres, C., Kappes, M., Johnsen, R. and Iannuzzi, M.** s.l. : NACE-International. , (2018). .

[38] *Effects of Tungsten on Corrosion and Kinetics of Sigma Phase Formation of 25% Chromium Duplex Stainless Steels. .* **Kim, J. and Kwon, H. (1999).** s.l. : CORROSION.

[39] *Effect of alloyed Mo and W on the corrosion characteristics of super duplex stainless steel weld. .* **H.J. and Lee, H.W.** s.l. : Int. J. Electrochem. Sci, (2014). .

[40] *Duplex stainless steels: microstructure, properties and applications. .* **Gunn R, editor.** s.l. : Woodhead publishing;, 1997 Oct 21.

[41] *Corrosion prevention and protection—Materials selection—Duplex stainless steels.* **Notten, G.** s.l. : Stainless Steel World, (2007). .

[42] *The corrosion of Superduplex stainless steel in different types of seawater. .* **Francis, R., Byrne, G. and Warburton, G.** s.l. : NACE International., (2011). .

[43] *Super duplex stainless steels. .* **JO., Nilsson.** 8(8):685-700., s.l. : Materials science and technology. , 1992 Aug 1;.

[44] *The corrosion resistance of duplex stainless steels. In Proc. Conf. Duplex Stainless Steels .* **Bernhardsson, S.** (1991). .

[45] *Corrosion of duplex stainless steels in seawater. .* **Wallén, B.** . (1998).

[46] *The influence of copper and.* **Bonfield, Jack.** s.l. : Swansea University, 2019.

[47] *Dependence of the critical pitting temperature on surface roughness. .* **Moayed MH, Laycock NJ, Newman RC.** s.l. : Corrosion science. , 2003 Jun 1;. 45(6):1203-16..

[48] *Effect of surface roughness on pitting corrosion of 2205 duplex stainless steel investigated by electrochemical noise measurements. .* **Tang Y, Dai N, Wu J, Jiang Y, Li J.** 12(5):738., s.l. : Materials. , 2019 Mar 4;.

[49] *The initiation of crevice corrosion in stainless steels. .* **Laycock, N., Stewart, J. and Newman, R.** s.l. : Corrosion Science,, (1997). .

[50] *Effect of pH and NaCl concentration on the corrosion of duplex stainless steel. .* **Prawoto, Y., Ibrahim, K. and Wan Nik, W.B.** s.l. : Arabian Journal for Science and Engineering, (2009). .

[51] *Effect of Tungsten and Nickel Addition on the Repassivation Behavior of Stainless Steel. .* **Kim, J., Xiang, P. and Kim, K.** s.l. : CORROSION, (2005). .

[52] *In situ monitoring of corrosion mechanisms and phosphate inhibitor surface deposition during corrosion of zinc–magnesium–aluminium (ZMA) alloys using novel time-lapse microscopy.* **Sullivan, J., Cooze, N., Gallagher, C., Lewis, T., Prosek, T. and Thierry, D.** s.l. : Faraday Discussions, (2015).